POLITECNICO
MILANO 1863

SCUOLA DI INGEGNERIA INDUSTRIALE
E DELL'INFORMAZIONE

Inter-Satellite Link based Relative Navigation for Spacecraft Formation Flying

Tesi di Laurea Magistrale in
Space Engineering - Ingegneria Spaziale

Author: **Francesco De Cecio**

Student ID: 948145
Advisor: Prof. Michèle Roberta Lavagna
Co-advisors: Dott. Stefano Silvestrini
Academic Year: 2021-2022

Abstract

Spacecraft formation flying missions are becoming more and more popular in the current years for different reasons. First, distributed systems allow for increasing the missions' scientific return. Moreover, they enable interferometric, stereoscopic and SAR imaging techniques with unprecedentedly large baselines. Both large formations in Earth orbit or deep-space one fall beyond the capabilities of the traditional ground-based control scheme. Therefore, the interest in autonomous formation maintenance is constantly growing. For this purpose, it is essential to provide a communication channel between the platforms by optical or RF link.

This thesis addresses the possibility of using inter-satellite RF link techniques to perform relative navigation in CubeSat formation flying missions. An overview of the available ranging methods is presented along with the mathematical models of the more promising ones, including the inherent signal transmission delays.

Moreover, an Extended Kalman Filter for both absolute and relative navigation is developed to assess the accuracy of the selected approaches. These include *indirect GNSS* and *direct one-way ranging*. Finally, different mitigation strategies have been developed for the most significant errors, and their impact on performance improvement is assessed.

The results show a higher relative navigation accuracy when employing inter-satellite distance measurements with respect to a traditional GNSS-only scheme. Furthermore, it is shown that transmission delays can significantly affect navigation accuracy and that the proposed correction strategy is effective. Lastly, the possibility of performing autonomous relative navigation in LEO with onboard generated signals for one-way ranging has also been confirmed.

Keywords: spacecraft formation flying, relative navigation, inter-satellite link, GNSS navigation

Abstract in lingua italiana

Le missioni che impiegano il volo in formazione di veicoli spaziali stanno diventando sempre più popolari negli ultimi anni. In primo luogo, l'impiego di sistemi distribuiti contribuisce ad aumentare il ritorno scientifico delle missioni. Inoltre, essi consentono l'utilizzo di tecniche di imaging interferometrico, stereoscopico e SAR con una distanza di base altrimenti irraggiungibile. Sia le grandi formazioni in orbita terrestre che quelle nello spazio profondo sono al di fuori delle possibilità del tradizionale schema di controllo da terra. Pertanto, l'interesse per il mantenimento autonomo delle formazioni è in costante crescita. A questo scopo, è essenziale fornire un canale di comunicazione tra le piattaforme tramite un link ottico o a radiofrequenza.

Questa tesi affronta l'applicabilità di tecniche di collegamento RF intersatellitare per eseguire la navigazione relativa in missioni CubeSat. Viene presentata una panoramica dei metodi di ranging disponibili e i modelli matematici dei più promettenti, comprendenti i ritardi intrinseci di trasmissione del segnale.

Inoltre, viene sviluppato un filtro di Kalman esteso per la navigazione assoluta e relativa, al fine di valutare l'accuratezza degli approcci selezionati. Questi includono i cosiddetti *GNSS indiretto* e *ranging diretto unidirezionale*. Infine, sono state sviluppate diverse strategie di mitigazione per gli errori più significativi ed è stato valutato il loro impatto sul miglioramento delle prestazioni.

I risultati mostrano una maggiore precisione di navigazione relativa rispetto a uno schema tradizionale basato solo sul GNSS quando si aggiungono misure di distanza intersatellitare. Inoltre, si dimostra che i ritardi di trasmissione possono influenzare significativamente l'accuratezza della navigazione e che la strategia di correzione proposta è efficace. Infine, è stata confermata la possibilità di effettuare una navigazione relativa autonoma in LEO con ranging unidirezionale a partire da segnali generati a bordo.

Parole chiave: volo spaziale in formazione, navigazione relativa, collegamento intersatellitare, navigazone GNSS

Contents

1 | Introduction

Since the dawn of space exploration, man has aimed to push the boundaries of knowledge, both in physical and technological terms, in a constant challenge to himself. Under the impetus of continuous improvement and driven by previous achievements, we have gone from pioneering research missions to exploiting entire constellations of satellites, even mass-produced, for commercial applications.

This paradigm shift goes hand in hand with the trend towards miniaturisation and modularity dictated by the advent of the CubeSat standard. In particular, what was once the prerogative of massive monolithic satellites can now be optimally performed by a CubeSat formation, allowing not only a significant reduction in costs and design time but also expanding the panorama of scientific possibilities.

With access to space now democratic, within reach of universities and small research centres, the possibility of developing formation flight missions, once the preserve of space agencies, is gaining ground. Together with it, the need for formation navigation and control solutions is also growing. This thesis aims to begin exploring the possibilities of making these formations independent and autonomous in space navigation, both to ground stations and external systems like GNSS.

1.1. Context & Motivation

The advantages of spacecraft formation flying are related to the fact that it is generally convenient to use multiple cooperating platforms rather than relying on a single much larger satellite. Benefits include cost reduction, faster design, and higher redundancy at a platform level since every spacecraft can be potentially replaced. Moreover, the formation geometry can be exploited for scientific purposes in applications like interferometric, SAR and stereoscopic imagery with unprecedented resolution [1].

This approach creates the need for a navigation technique that can estimate not only the absolute state of each spacecraft but also the relative state of the whole formation, i.e. the relative positions and velocities of each component with respect to the others.

This task is propedeutic to formation control and maintenance, which can be executed in two ways:

- **Ground-based control.** In this case, the measurements collected by each spacecraft are sent to the ground, where they are processed to retrieve the relative state and calculate the needed adjustments. Once this has been performed, eventual manoeuvre commands are uploaded on each spacecraft;
- **Autonomous control.** In order to perform autonomous formation maintenance, the collected measurements are broadcasted between all the platforms to execute relative state estimation, following a centralised or distributed scheme. Then, each spacecraft decides autonomously if there is the need to perform an adjustment manoeuvre.

This second alternative is much more challenging and is the object of research due to its enormous potential. For example, it can allow deep-space applications and large constellations control, both tasks beyond ground-based control capabilities.

In this case, the whole navigation chain - from relative measurements production and exchange to relative state estimation - shall be performed on board. Hence, it is mandatory to establish a communication channel between the formation flying spacecraft whose task is twofold. First, it makes it possible to exchange navigation data for relative state estimation. Second, it plays a role in the scientific mission, allowing data transmission between platforms and thus enabling cooperative scientific operations.

Two main alternatives for doing this are radio frequency and optical inter-satellite links (ISL). While the performances of the optical ISL are extremely promising, it is still challenging to implement them on low-budget missions since they require more sophisticated devices and very accurate pointing. RF solutions are instead cheap and reliable enough to be considered in almost all mission classes, albeit being characterised by lower performances [2, 3].

This thesis is devoted to exploring the techniques currently available for performing RF ISL-based relative navigation in a CubeSat formation, taking as a reference case the VULCAIN mission described in the following section.

1.2. VULCAIN mission scenario

VULCAIN is a mission proposal under development at Politecnico di Milano, with the collaboration of the Italian Space Agency (ASI) and the Italian National Institute for

Geophysics and Vulcanology (INGV), for volcanoes monitoring purposes. The mission aims to acquire multispectral stereoscopic images of selected volcanoes with high spatial resolution. The stereographic acquisition of the areas of interest will be achieved by employing a formation flying architecture composed of two satellites.

Two 12U CubeSats are under consideration for performing these tasks. The proposed trailing formation features a very low-altitude circular orbit with variable along-track separation, allowing it to meet evolving scientific requirements.

The mission will implement standard techniques to retrieve relative navigation from absolute navigation and ground ranging. At the same time, it also aims at demonstrating innovative techniques for relative navigation based on a UHF inter-satellite link.

1.3. Thesis contributions

This thesis aims to understand how it is possible to navigate a formation of spacecraft exploiting an inter-satellite link between them.

A survey of the ranging methods that exploit this communication channel is performed to identify the viable alternatives for the VULCAIN mission. Both measurement and dynamics models are reviewed and categorised. An estimate of the achievable accuracy of each technique is sought, together with its impact on the overall navigation process. Moreover, the identification of the main sources of error has been addressed.

To guide this work, the following research questions are formulated:

1. Is it possible to navigate a CubeSats formation by exploiting an ISL between them?
2. What are the available methods to perform ranging measurements by exploiting a radio frequency ISL?
3. Do ranging measurements improve the accuracy of a traditional GNSS-based navigation filter?
4. What are the main errors that affect navigation accuracy?
5. Is it possible to perform range-only relative navigation?

The last chapter of this document will try to answer these questions based on the evidence collected and the results obtained.

1.4. Thesis outline

Here is briefly presented the structure of this thesis work. The following paragraphs summarise the topic of each chapter of the document.

Chapter 2 It is devoted to presenting the ranging techniques that make use of an inter-satellite link. It represents a literature review to classify the available methods according to their working principles. It contains some considerations about the advantages and disadvantages of each of them, along with their flight heritage.

Chapter 3 It describes how relative measurements can be employed in a state estimation procedure. First, the mathematical models of the most significant techniques are developed, including a discussion of the typical errors that affect each. Then, the available dynamics models are reviewed to understand which ones are the most suitable for being used in a navigation algorithm of a VULCAIN-like formation.

Chapter 4 An implementation of an Extended Kalman Filter for both absolute and relative state estimation is proposed in this chapter. The developed measurement models are employed here for state updates. The purpose is to create a simple and versatile tool that can be used, through appropriate simulations, to assess the performances of different navigation strategies.

Chapter 5 A simulation framework for testing the performance of the proposed EKF is here presented. The test scenario, inspired by the VULCAIN mission, is described. A high-accuracy ground-truth model is presented and used to propagate the reference trajectories. The procedure for measurement generation is also described, reporting the numerical values of the coefficients needed for this task. Finally, the adopted performance comparison procedure is discussed.

Chapter 6 The filter's performances in absolute and relative navigation are reported and discussed in this chapter. The accuracy of different ranging techniques, the impact of delayed measurements, and the effectiveness of error mitigation strategies are assessed. The possibility of performing range-only relative navigation is also investigated.

Chapter 7 This chapter summarises the most relevant facts that have emerged from the analyses reported in this document. It tries to answer the research questions that have driven the work and presents the next steps needed to consolidate these findings and eventually arrive at an implementation phase.

2 | Inter-Satellite Ranging Techniques

This chapter aims to organise all the techniques available in the literature for carrying out ranging measurements using RF signals. First, each of them is described to identify its peculiarities, allowing to point out its advantages and disadvantages. Then, the flight heritage is presented to better understand the maturity of these techniques. Finally, those most suitable for application in the scenario described in Chapter 1 are highlighted.

2.1. Overview of ranging techniques

The objective of a ranging system employed in the relative navigation of a satellite formation is to provide all platforms with a measure of the distance separating them from each other. In other words, the aim is to create a device capable of exploiting an RF channel between the various satellites in the formation to estimate the inter-satellite distance. There are multiple ways of doing this. In particular, inter-satellite ranging methods can be categorized into two main families: direct and indirect methods [2].

Indirect methods This class of techniques exploits ISL only for exchanging absolute measurements between the platforms. There is no active role of the RF signals in the measurement process, but they are only used as a communication channel. In this case, the relative measurements are obtained by subtracting two absolute measurements. These latter shall be brought, in turn, from external systems like GNSS or ground station tracking.

Direct methods Conversely, direct methods actively exploit the signal to measure the distance between the transmitting and receiving spacecraft. Generally, distance can be inferred from time or phase measurements made on the signal. They have the advantage of being independent of external systems, enabling fully-autonomous relative navigation. Moreover, higher accuracy levels can be reached by adopting this strategy. Depending

on the adopted measurement scheme, they are further classified into one and two-way ranging methods.

The following sections will explore the two families, presenting the alternatives that constitute each.

2.2. Indirect ranging

The indirect ranging methods retrieve relative quantities from absolute measurements exchanged via ISL between the platforms. These products come from external systems and can be either processed or raw.

The most widely used method to perform ranging in this way relies on absolute GNSS measurements made by both spacecraft, exchanged and finally differenced, allowing the indirect computation of the relative position and velocity of the formation.

GNSS data can also be used in raw format in the so-called carrier-phase differential GPS (CDGPS) [4]. Initially developed for the GPS system, this approach involves using raw carrier-phase observables from a GNSS receiver to form differenced measurements, allowing direct estimation of the inter-satellite distance. It has the advantage of reducing (or even eliminating) common error sources between platforms, such as the GPS satellite clock offsets and common biases due to hardware delays. According to how observables are combined, it is possible to form the following quantities:

- **Single differences:** are formed by subtracting two GPS observations of the same type and on the same frequency, taken by two GPS receivers at the same instant and originating from a mutually observed GPS satellite;
- **Double differences:** are formed by subtracting two single difference observations of the same type and frequency, taken by the same two GPS receivers at the same instant, each relating to a different GPS satellite.

This method can reach high precision levels and does not require additional hardware to be put in place. Measurements are collected by the same GNSS receiver used for absolute navigation and sent to the other platform via ISL. The onboard navigation processor will then form the desired differences, which will be used to perform the relative position estimation.

In addition to GNSS, the absolute position data needed to perform indirect ranging can be obtained by different systems. These include ground station tracking, TDRSS tracking, PRARE tracking and TLEs.

2.3. Direct ranging

In this class of methods, the onboard transceivers play an active role in generating and analysing the ranging signals. Processing them makes it possible to retrieve the range, either through a time or a phase measurement.

If this latter is employed, the achievable accuracy is enough to allow not only ranging but also Line of Sight (LOS) vector estimation (in terms of azimuth and elevation angles). However, doing this requires an array of multiple antennas on each LOS estimating platform. It is indeed required to collect the phase of the incoming wave at different points and process their difference. This technique is also known as angle of arrival (AoA) measurement.

Depending on whether the measurements are made by the receiving spacecraft or whether the signals are transmitted back to the sender and measured there, it is possible to distinguish one-way or two-way ranging. In any case, a dedicated device shall be employed to perform these tasks, increasing design complexity but also autonomy and accuracy compared to indirect methods.

2.3.1. One-way ranging

In this measurement scheme, a signal is generated from one S/C of the formation and transmitted. When received by the others, the distance measurement is performed. There are several ways to do that:

GNSS-like It uses a signal with the same structure as the one used by GNSS constellations but is locally generated onboard [5]. More precisely, it is a pseudorandom noise (PRN) code modulated onto a carrier wave. Two measurements are possible: a time one, the pseudorange, which is coarse but not ambiguous, and the carrier-phase, more accurate but ambiguous. Despite having a significant heritage, this method requires precise (and challenging) clock synchronisation between the two platforms if high accuracy is desired.

Received Signal Strength Indicator (RSSI) It is a method based on measuring the attenuation of a signal of known initial power through the wireless channel to estimate the transmitter-receiver distance [6]. It is very simple but rather inaccurate, especially for long baselines.

Time Delay of Arrival (TDOA) This technique is based on measuring the time difference in the signal's arrival at two different receivers whose position is known. If the

receivers' clocks are synchronised, the time difference is proportional to the distance from the transmitter.

Range rate (Doppler shift) The Doppler shift of the received signal from the original carrier frequency can be used to compute the range rate. Even if it does not provide a direct range measurement, this latter can be obtained by processing its rate with an estimator.

2.3.2. Two-way ranging

In this case, the satellite that sends the ranging signal activates a counter to calculate the elapsed time until it receives the same signal transmitted back by the other spacecraft. Since the transmission and the measurement are performed on the same platform, there is no need for clock synchronisation. The relay spacecraft can re-transmit the same signal it has received or apply a so-called turnaround ratio to its frequency, allowing simultaneous transmission and reception by frequency division multiple access (FDMA).

Various TWR schemes are available like Single-Sided, Symmetric Double-Sided, Alternative Double-Sided and Asymmetric Double-Sided. The reader interested in deepening the differences between them should refer to Lian Sang's work [7].

2.4. Flight heritage

This section discusses the flight heritage of the presented techniques by providing a small description of the missions that exploited each kind of method.

2.4.1. Indirect methods heritage

Almost every formation flying mission in LEO equipped with GNSS receivers and ISL capabilities (e.g. GRACE, PRISMA) made use of CDGPS technology to perform relative navigation. Some missions, introduced in the following paragraphs, relied exclusively on this technique for relative state estimation.

TanDEM-X It is a high-resolution SAR mission composed of two radar satellites flying in close formation to achieve the desired interferometric baselines in a highly reconfigurable constellation [8]. The formation's control is done autonomously onboard by the TAFF system [9, 10]. It features an S-band ISL, and its maximum inter-satellite range has been 5 km.

CanX-4/5 It is a dual-nanosatellite formation flying demonstration mission to prove that formation maintenance could be accomplished with sub-meter error accuracy on small platforms [11]. It features an S-band ISL with a data rate of 10 $kbits/s$, and its maximum inter-satellite range has been 5 km.

2.4.2. One-way methods heritage

Among the one-way methods, GNSS-like ISR is a mature and reliable technology. It has been applied to several missions, as described in the following paragraphs.

GRACE It is a dual-minisatellite geodetic mission with the overall objective of mapping accurately the Earth's gravity field. Its KBR instrument is a K/Ka-band DOWR (Dual one-way ranging) system that allows a micrometre-level accuracy ranging [12]. Each of the two satellites transmits a carrier signal and compares it with the received one (generated by the other satellite). Operating in K-band, this system requires considerable transmission power due to free path losses. Clock synchronization relies on GPS time tags [13].

GRAIL The mission is meant to map the moon's gravity field and is based on GRACE technologies. Operating outside GPS coverage, it is coupled with an S-band time-transfer link for clock synchronization purposes.

PRISMA It is a technology mission to demonstrate formation flying and rendezvous technologies. It comprises a master spacecraft, MANGO, and a slave one, TANGO. It features a dual-frequency S-band communication link and a set of seven antennas on each S/C (FFRF subsystem). The distance and the line of sight between the platforms are calculated employing inter-satellite pseudorange and carrier-phase measurements.

ST-5 It is a NASA mission to test innovative concepts and new technologies for future missions in a constellation of three spacecraft. It has served as a precursor to MMS. Its CCNT S-band transponder can generate and interpret a GPS-like pseudo-random noise (PRN) code, process carrier phase and Doppler measurements.

MMS It is a solar-terrestrial probe constellation comprising four identically instrumented spacecraft that will use Earth's magnetosphere as a laboratory to study the microphysics of plasma processes. An S-band ISL with a very broad range, up to 3500 km, enables GNSS-like relative ranging [14].

PROBA-3 Planned to be launched in 2023, this mission wants to demonstrate the technologies required for the formation flying of multiple spacecraft in the fields of space science, Earth Observation and surveillance. It features the so-called GAMALINK UHF to S-band ISL, configurable according to scientific, communication and power consumption requirements.

2.4.3. Two-way methods heritage

Two-way ranging methods are exploited mainly by spacecraft tracking systems both from ground stations and from space. Some examples are:

TDRSS The Tracking and Data Relay Satellite System (TDRSS) is a network of American communications satellites and ground stations used by NASA for space communications. It allowed both one and two-way ranging of the client satellites connected to the network [15].

PRARE It was a microwave tracking system active on board the ERS-1 and ERS-2 missions. It operated at centimetre accuracy levels for the measurement of satellite-to-ground range and range rate. The concept was based on an autonomous spaceborne two-way and dual-frequency microwave tracking system [16].

MMS This already cited mission could also perform two-way ranging measurements between companion spacecraft [14].

Several authors also propose using two-way ranging in an emitter-reflector configuration between two formation-flying spacecraft. Two examples are reported in the following paragraphs.

DTR It is a dual transponder ranging system designed to overcome the requirement of precise clock synchronization while performing high-accuracy ranging [17].

IDST It is a proposal to obtain similar performances of the GRACE mission DOWR with simplified hardware, partially shared with the TMTC subsystem [18].

2.5. Applicability to a CubeSat mission

Among the technologies presented in the previous sections, some are particularly suited for the context of a CubeSat mission, with particular reference to VULCAIN.

The most simple and reliable one is the indirect ranging based on the exchange of processed GNSS measurements. Not only can it count on a solid heritage (since using a commercial GNSS receiver), but it does not require any additional hardware apart from the RF transceiver used for establishing a communication channel between platforms. Moreover, it allows at the same time to estimate both relative position and relative velocity because the receiver can obtain both absolute measurements. For this reason, even if the achievable accuracies are low, it represents a complete, robust, and cost-effective solution for small platforms' absolute and relative navigation.

CDGPS, using GNSS raw absolute measurements to extract accurate relative estimates, is also very interesting for CubeSats applications. Moreover, the heritage of the CanX-4/5 mission is significant. However, this system suffers from the identical major drawback of the previous technique, i.e. relying entirely on GNSS coverage.

Therefore, if one needs to employ a system that can operate in different scenarios (e.g. deep space or full autonomy), the focus must be put on other methods. Considering the potential performance and heritage of the presented technologies, GNSS-like one-way ranging and time-of-flight two-way ranging are the most promising ones. The first is more suitable for a distributed formation architecture, allowing every spacecraft to send and process ranging signals. The second is instead more suited for a master-slave centralised design, where only the master spacecraft is in charge of performing the formation's relative navigation.

3 | Inter-Satellite Link based Navigation Methods

This chapter aims to explain how and when the ranging techniques presented in Chapter 2 can be employed for navigation purposes. When operating two or more spacecraft flying in a formation, an Inter-Satellite Link can be beneficial from several points of view:

- Allows a higher degree of autonomy in formation maintenance and control since relative state estimation can, in this case, be performed onboard without relying on ground-based relative navigation or GNSS constellations;
- Enables real-time relative navigation with unparalleled precision by mutual observables sharing and co-processing.

Considering the scenario presented in Sec. 1.2, some of the most promising approaches have been modelled for these purposes, and their applicability to a navigation filter is discussed in the following sections.

3.1. Overview of relative navigation methods

Generally speaking, there are two ways to perform relative navigation, each requiring suitable measurements and dynamics models. The following paragraphs represent an introduction to both these alternatives, along with a brief characterisation regarding their advantages and disadvantages.

Absolute-based navigation It is possible to retrieve the formation's relative state by subtracting the absolute states of the member spacecraft. This approach is undoubtedly efficient since it requires nothing more than the absolute navigation solutions, which are typically already available in the guidance computer of each spacecraft and can conveniently be obtained, for example, by a simple off-the-shelf GPS receiver. However, since relative quantities are derived from absolute measurements affected by errors, their combination generally produces a more significant error. The main advantages are thus

reliability and heritage, while the disadvantages are limited autonomy and accuracy.

Direct relative navigation In this case, the measurement and dynamic model are intrinsically relative. This method family represents a more independent alternative since it does not require external players once the system observability is guaranteed. In addition, contrary to the above, measurement accuracy is automatically reflected in estimation accuracy. On the other hand, precise relative dynamic models are more challenging to implement and often require an absolute reference trajectory.

Hybrid approaches exist between these extremes, combining the absolute and relative worlds. In particular, relative measurements can be used to improve the performance of absolute-based relative navigation, as demonstrated in Sec. 6.2.3.

In both cases, data processing can occur according to a centralised or decentralised strategy. In the first case, the master spacecraft is the sole navigator and distributes the products to the slaves via ISL. While in the second, there is no such hierarchy, and each spacecraft is autonomous concerning the mentioned functions. This choice, which affects the system design of the formation, must be made considering that, on the one hand, it would introduce a single point of failure; on the other hand, it would complicate the design of the spacecraft. The slaves, in the latter case, must indeed be in all respects equal to the master.

Common to all techniques is the need to exchange either processed data or raw measurements between all platforms. Therefore, an ISL that can guarantee a reliable connection is indispensable in a relative navigation system that wants to be ground-independent. This implies that any information transmitted through the RF channel, due to the finite speed of light, will be received with an unavoidable delay proportional to the distance travelled (neglecting secondary effects discussed later). Accordingly, it is vital to consider these delays in the filter design and assess their impact on the overall navigation accuracy. Both these aspects will be detailed later in this thesis.

3.2. Measurement models

Two factors have guided the choice of which measurements models to develop:

- applicability to VULCAIN mission, discussed in Sec. 2.5;
- current heritage, discussed in Sec. 2.4.

In particular, two were selected among the ranging techniques presented in Chapter 2: indirect and GNSS-like direct ranging.

Indirect ranging This technique has been deemed mature and reliable enough to be selected for the relative navigation baseline. It can achieve adequate precision for loose formation control, requires little to no preprocessing, and has a strong heritage. Moreover, exploiting the already present GNSS receivers does not require any additional component apart from the ISL-related hardware.

GNSS-like direct ranging This technique has been selected to provide native relative data and to offer a GNSS constellations-independent solution for relative navigation. It requires additional hardware to generate and process ranging signals, as described in Sec. 2.3.1, and an ISL to exchange them between platforms. Operating in DOWR mode can also estimate the clock bias between the two platforms. There is a limited but significant heritage, especially for shorter baselines.

Each technique, as already mentioned, has its sources of error and, therefore, its achievable accuracy. It is necessary to comprehend the underlying physical principles to understand why there is a particular measurement error. Hence the modelling effort is essential in a twofold manner. On the one hand, it allows a realistic measurement simulation, allowing a performance assessment of the filter under study. On the other hand, a deeper comprehension of the error mechanisms allows for proposing a more effective error reduction technique, which can act deterministically to cancel out some of the most significant ones without even the need to estimate them.

Since the proposed methods rely on GNSS measurements, let us start by reviewing how a GPS receiver works and which are its typical observables to better understand the subsequently proposed measurement models.

3.2.1. Introduction on GNSS observables

Before going into measurement models, it is helpful to recall how a GPS receiver computes the user's position.

A modern receiver can receive signals at multiple frequencies and from different constellations. For example, Novatel OEM719 can process signals from GPS, GLONASS, Galileo, BeiDou, QZSS and IRNSS, offering sub-meter to centimetre level positioning. Common to most navigation constellations are the observables on which the positioning relies: pseudorange, carrier-phase, and Doppler shift. The following sections will explain the nature of the first two measurements and the methods used by the receiver to compute them. The reader interested in how these latter are employed to estimate the user's position and clock bias should refer to standard GPS textbooks such as [19] or [20].

3.2.1.1. Pseudorange

Pseudorange is computed as the time difference between signal transmission time (as measured by the transmitting GPS spacecraft's clock) and the reception time (as measured by the receiver's clock) multiplied by the speed of light.

$$\rho = c\,\Delta t = c\,[t_{Rec}(T_{RX}) - t_{Tran}(T_{TX})] \tag{3.1}$$

This procedure is made possible by the properties of a particular digital sequence, known as Pseudo Random Noise (PRN) code, which is modulated onto the GPS signal's carrier. Each GPS satellite transmits a different code, and a receiver shall thus be able to generate all the possible replicas to obtain the correct measurement. Critical properties of these binary sequences are a close-to-zero cross-correlation and an autocorrelation with a sharp peak in zero. Referring to Eq. (3.1), the receiver calculates the term Δt by correlating the incoming PRN code with a locally generated replica, which is shifted back and forth in time until the maximum correlation is reached, as shown in Fig. 3.1. Once recovered, the delay's tracking is demanded to a Delay Lock Loop (DLL), which guarantees continuous measurements until the transmitting GPS satellite is still in view.

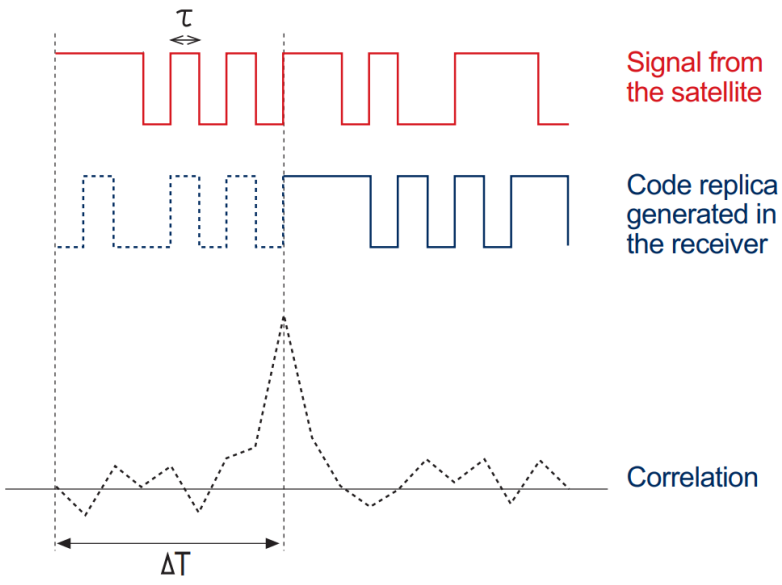

Figure 3.1: Determination of signal time-of-flight through correlation [21].

If the clock of the GPS satellite and the receiver were both synchronized to GPS reference time, and if there were no disturbances in the ionospheric propagation of RF signals, then the quantity $c\,\Delta t$ would correspond to the actual geometric range between the GPS satellite's position at transmission time and the receiver's position at reception time. Since

these assumptions are not generally valid, it is called *pseudo*range. In Sec. 3.2.3.1, typical errors and a proper modelling strategy will be presented in detail.

By simultaneously measuring the pseudorange from at least four satellites, the receiver can estimate the user's position and clock bias, following a least-squares approach described in [19].

3.2.1.2. Carrier-phase

Conversely to pseudorange, carrier-phase observable is not a time measurement but a phase one. It is calculated by measuring the carrier wave's phase at reception time. First, it is necessary to demodulate the received signal removing code and navigation data from it, thus recovering the raw carrier. Then it is mixed with a locally generated reference sinusoid, and the phase of the resulting signal is measured. This measure can be used in a Phase-Locked Loop (PLL) to track the phase variations of the received carrier.

Measuring a phase is much more accurate than correlating a code, meaning that a lower noise level and, consequently, higher accuracy can be achieved. Nevertheless, due to its periodicity, this observable is ambiguous by an unknown number of phase cycles. Moreover, this ambiguity changes every time the receiver loses the signal lock, introducing discontinuities in the measurements.

Once this ambiguity has been solved, a very accurate measure of the satellite-to-receiver distance is obtained and can be used for precise navigation.

3.2.2. Indirect ranging

This method, introduced in Sec. 2.2, calculates an estimate of the relative state that relies on differencing the user's position, velocity, and clock correction as computed by the GNSS receiver of each spacecraft. An active ISL is therefore needed to allow a mutual exchange of the processed absolute navigation solutions between platforms.

To model this technique, it has been assumed that each spacecraft transmit to its companion a message including:

1. position (ECI frame);
2. velocity (ECI frame);
3. measurement timestamp (obtained from the onboard clock, corrected by the clock bias estimated by the GNSS receiver).

Each component has been corrupted by an Additive White Gaussian Noise (AWGN) whose variance is selected from the employed receiver's datasheet. Considering a two-spacecraft formation, as in the case of the VULCAIN mission, the exchanged packets are thus in the form of Eq. (3.2). Only the measurements from spacecraft A are reported for conciseness.

$$GNSS_A = \begin{bmatrix} \mathbf{r}_A^{ECI} \\ \mathbf{v}_A^{ECI} \\ t \end{bmatrix} + \begin{bmatrix} \mathbf{w_r} \\ \mathbf{w_v} \\ w_t \end{bmatrix} \qquad \begin{matrix} \mathbf{w_{r,v}} \sim \mathcal{N}_3(\mathbf{0},\, \mathbf{\Sigma_{r,v}}) \\ w_t \sim \mathcal{N}_1(0,\, \sigma_t^2) \end{matrix} \tag{3.2}$$

The transmission is performed at regular time intervals that can be tuned according to a trade-off between needed accuracy, computational power and the receiver's characteristics.

It is pointed out that a transmission delay always exists between measurements collection and their usage by the navigation filter. Considering the onboard relative navigation filter of spacecraft A, it will only have access to spacecraft B's measurements at the time expressed in Eq. (3.3).

$$t_{RX} = t_{TX} + \Delta t_{BA}^{trn} \tag{3.3}$$

This delay is the sum of several factors involved in signal transmission, as discussed in the following section.

3.2.2.1. Transmission delay model

The transmission delay Δt^{trn} is the time between the emission of a signal and the moment when the transmitted information is available to the receiver. In this model, three contributions are accounted for, as described in the following paragraphs.

Time of flight It is the time it takes for a signal travelling at the speed of light to go from the transmitter antenna position to the receiver position. Mathematically, it can be expressed as:

$$\delta t_{BA}^{tof} = \frac{|\mathbf{r}_A(t) - \mathbf{r}_B(t - \Delta t_{BA}^{trn})|}{c} \tag{3.4}$$

Where c is the speed of light in vacuum.

Ionospheric delay The presence of charged particles in the ionosphere affects the propagation of an RF signal travelling through its layers. The main contribution is given by free electrons encountered in the propagation path, specifically on the Total Electron Content (TEC). In particular, a modulated signal travels slower in the ionosphere than in free space. The excess propagation time is called group delay and can be computed as:

$$\delta t_{BA}^{ion} = \frac{40.3}{c\, f^2}\, TEC_{BA} \tag{3.5}$$

Where c is the speed of light in vacuum and f is the carrier frequency. A more exhaustive discussion of ionospheric effects is reported in Sec. 3.2.5.

Line bias This term accounts for the time required from the signal's arrival at the receiving antenna to its complete decoding. The most significant source of bias is the intrinsic delay introduced by the analogue RF filters used in signal processing. It has been modelled as a constant term δt^{ln}, and its value differs for each receiver.

The total transmission delay from spacecraft A to spacecraft B is thus modelled as follows:

$$\Delta t_{BA}^{trn} = \delta t_{BA}^{tof} + \delta t_{BA}^{ion} + \delta t_{A}^{ln} \tag{3.6}$$

3.2.3. Direct GNSS-like one-way ranging

The concept behind this ranging method has been explained in Sec. 2.3.1. It employs a signal with the same structure as the GNSS one, making it possible to produce the usual pseudorange and carrier-phase observables (in this case, these are a direct measure of the inter-satellite distance). The only difference with GNSS is that signals are generated onboard each spacecraft, and thus each can measure its distance from the other, paving the way to Dual One-Way Ranging.

A measurement model for both observables has been derived based on a modified version of the model proposed by Psiaki for CDGPS [22]. For conciseness, all the equations of the following sections are written for signals generated in spacecraft B, received and processed in spacecraft A.

3.2.3.1. Pseudorange measurement model

It is a one-way time of flight measurement obtained by correlating PRN codes, as described in Sec. 3.2.1.1. The employed measurement model accounts for the ionospheric delay and

line bias, already presented in Sec. 3.2.2.1 and clock errors of both platforms.

It shall be considered that this system can operate in the absence of GNSS coverage (and thus without its time corrections). In this scenario, onboard clocks drift rapidly due to their frequency instability, causing potentially unbounded errors. A model for this drift is presented in Sec. 3.2.4, while potential solutions will be discussed later in Sec. 4.4.2.

Denoting:

$$t_A = t + \delta t_A \qquad t_B = t + \delta t_B \tag{3.7}$$

Where $t_{A,B}$ are the times measured by the respective onboard clocks, and t is true time. The pseudorange model can be written in the form of Eq. (3.8).

$$\rho_{BA}(t) = |\mathbf{r}_A(t) - \mathbf{r}_B(t - \Delta t^{trn}_{BA})| + c\,(\delta t_A - \delta t_B) + c\,\delta t^{ion}_{BA} + c\,\delta t^{ln}_A + \varepsilon^{th}_\rho \tag{3.8}$$

Where ε^{th}_ρ is the receiver's pseudorange thermal noise whose standard deviation is given by:

$$\sigma_{\varepsilon_\rho} = c\,t_c \sqrt{\frac{B_{\mathrm{DLL}} t_{\mathrm{eml}}}{2 t_c C/N_0} \left(1 + \frac{1}{t_{\mathrm{acc}} C/N_0}\right)} \tag{3.9}$$

Being generated in the RF signal processing, it is determined by the features of the employed DLL. In particular: C/N_0 is the received carrier-to-noise ratio in dB Hz, B_{DLL} the DLL bandwidth, t_{eml} the time spacing between the early and late code replicas used in the DLL's correlator, t_c the chipping period of the PRN code, and t_{acc} the pre-detection integration time of the accumulations used in the DLL's discriminator.

3.2.3.2. Carrier-phase measurement model

Following an analogous procedure to the one presented in Sec. 3.2.1.2, this system can measure the phase of the incoming carrier wave with good precision. This technique is, however, more sensible to deterministic errors since it is characterised by a much lower noise level. The following paragraphs are devoted to a description of the more significant ones.

Ionospheric phase advance The ionosphere does not introduce only a time delay in the modulated signals travelling through its layers but also causes a phase advance in

their carrier. While a more detailed discussion is presented in Sec. 3.2.5, the carrier-phase advance can be modelled through the δt_{BA}^{ion} term presented in Sec. 3.2.2.1.

$$\delta\phi_{BA}^{ion} = f\,\delta t_{BA}^{ion} \tag{3.10}$$

Where f is the carrier frequency.

Phase windup If a circular polarisation is chosen for the signal, this can result in a perturbation known as phase windup $\delta\phi_{\mathrm{A}}^{\mathrm{pwu}}$. A constantly increasing term will bias the phase measurement if the receiving antenna spins about its boresight.

Multipath This perturbation $\delta\phi_{\mathrm{A}}^{\mathrm{mp}}$ is caused by signal reflection on spacecraft surfaces, causing an error in phase measurement when reflected signals are fed into the receiving antenna. It depends on the spacecraft's geometry and attitude.

Antenna phase-centre variations The apparent radiation source in an RF system is called the antenna phase-centre. It does not coincide with its geometrical centre but depends on the propagation direction and signal frequency. It is difficult to predict its position precisely, and since phase measurements are referred to it, this introduces a perturbation $\delta\phi_{\mathrm{A}}^{\mathrm{pc}}$.

The complete carrier-phase measurement model is finally obtained, starting from the time history of the transmitted carrier wave's phase (as generated by the emitter spacecraft B):

$$\psi_B(t_B) = \psi_B^0 + f\,t_B(t^{TX}) \tag{3.11}$$

Where ψ_B^0 is the phase at the beginning of the transmission epoch.

Once arrived at the receiver, after Δt_{BA}^{trn} seconds, this phase appears modified in the following form, accounting for transmission delay and each perturbation described in the previous paragraphs.

$$\psi_B(t_B) = \psi_B^0 + f\,(t_B(t^{RX}) - \Delta t_{BA}^{trn}) + 2f\,\delta t_{BA}^{ion} + \delta\phi_{\mathrm{A}}^{\mathrm{pwu}} + \delta\phi_{\mathrm{A}}^{\mathrm{mp}} + \delta\phi_{\mathrm{A}}^{\mathrm{pc}} + \varepsilon_{\phi}^{th} \tag{3.12}$$

Please note that the factor 2 in the ionospheric phase advance term is needed to compen-

sate for the presence of δt_{BA}^{ion} inside Δt_{BA}^{trn} transmission delay. Moreover, ε_{ϕ}^{th} is the thermal noise associated with the PLL processing, and its standard deviation can be expressed, in cycles, as:

$$\sigma_{\varepsilon_\phi} = \frac{1}{2\pi}\sqrt{\frac{B_{\text{PLL}}}{2C/N_0}} \tag{3.13}$$

Where C/N_0 is the received carrier-to-noise ratio in dB Hz, B_{PLL} the PLL bandwidth.

The receiver's replica, at the time instant when the signal described by Eq. (3.12) is received, reads:

$$\gamma_A(t_A) = \gamma_A^0 + f\, t_A(t^{RX}) \tag{3.14}$$

Where γ_A^0 is the replica's phase at the beginning of the incoming phase tracking epoch.

The actual carrier-phase observable is the difference between the replica in Eq. (3.14) and the received phase in Eq. (3.12).

$$\phi_{BA}(t_A, t_B, t^{RX}) = \gamma_A(t_A) - \psi_B(t_B) \tag{3.15}$$

To obtain a measurement in meters, Eq. (3.15) shall be multiplied by the carrier's wavelength λ. Having that done, it is interesting to expand the result. Recalling $c = \lambda f$ and rearranging the terms, the equation yields the typical carrier-phase measurement model found in textbooks.

$$\begin{aligned}\Phi_{BA}(t) = \lambda\,\phi_{BA} = |\mathbf{r}_A(t) - \mathbf{r}_B(t - \Delta t_{BA}^{trn})| + c\,(\delta t_A - \delta t_B) + \lambda\,(\gamma_A^0 - \psi_B^0) \\ - c\,\delta t_{BA}^{ion} + c\,\delta t_A^{ln} - \lambda\,(\delta\phi_{\text{A}}^{\text{pwu}} + \delta\phi_{\text{A}}^{\text{mp}} + \delta\phi_{\text{A}}^{\text{pc}} + \varepsilon_{\phi}^{th})\end{aligned} \tag{3.16}$$

In this expression, it is worth pointing out two things. The first one is that the ionospheric term shows here a minus sign, conversely to the pseudorange model in Eq. (3.8). This means a shorter phase is measured for a signal travelling through the ionosphere than what it would have been on the same free-space path.

The second interesting thing is the fourth term of the expression. It represents the difference between the two initial phases of the received signal and its replica. This term is entirely arbitrary and depends upon the design of the RF equipment. For this reason,

there is no way to estimate its value from carrier-phase measurements only. This is why it is often referred to in the literature as carrier-phase ambiguity. Moreover, whenever the signal transmission is interrupted, or tracking is lost, its values could change, introducing discontinuities in the measurements.

Concluding, albeit the estimation of this ambiguity is somehow challenging, once this is achieved, carrier-phase measurements can reach cm to mm accuracy.

3.2.4. Clock error model

Each satellite is equipped with an onboard clock, whose stability plays a fundamental role in navigation applications. Generally speaking, these devices need periodic calibrations to keep the positioning error low. As can be seen from pseudorange and carrier-phase measurement models, clock errors from both spacecraft negatively affect the observables.

There is thus an interest in quantifying these deviations for two main reasons. First, a tool for assessing the clock's performance in a navigation system via numerical simulations is needed. Second, an accurate model could be employed in the navigation filter to remove the clock-related bias.

Recalling Eq. (3.7) a model is therefore needed for $\delta t_{A,B}$. It is common to employ the so-called two-state model [23], which is a double integrator driven by two white noise terms, as shown in Fig. 3.2. The discrete version of the model, presented in [24], is reported below. For spacecraft A it reads:

$$\begin{bmatrix} \delta t_{\mathrm{A}(k+1)} \\ \delta f_{\mathrm{A}(k+1)} \end{bmatrix} = \begin{bmatrix} 1 & \Delta t_k \\ 0 & 1 \end{bmatrix} \begin{bmatrix} \delta t_{\mathrm{A}(k)} \\ \delta f_{\mathrm{A}(k)} \end{bmatrix} + \begin{bmatrix} \sqrt{S_f \Delta t_k + \frac{S_g \Delta t_k^3}{12}} & \sqrt{\frac{S_g \Delta t_k^3}{4}} \\ 0 & \sqrt{S_g \Delta t_k} \end{bmatrix} \mathbf{w}_{A(k)} \tag{3.17}$$

Where $\Delta t_k = t_{k+1} - t_k$ is the simulation's discrete time step and $\mathbf{w}_{A(k)} \sim \mathcal{N}_2(\mathbf{0}, \boldsymbol{I}_2)$ is a Gaussian white noise with zero mean and identity covariance.

Clock's phase and frequency drift intensity, namely S_f and S_g, are approximated as:

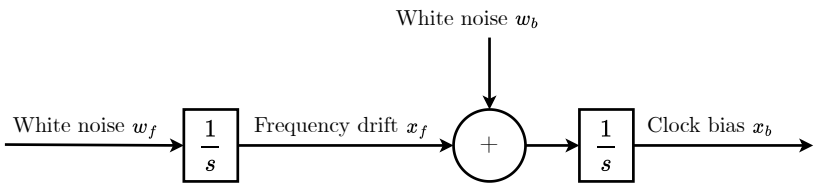

Figure 3.2: Two-state clock error model.

$$\begin{aligned} S_f &\approx \tfrac{1}{2}\, h_0 \\ S_g &\approx 2\pi^2\, h_{-2} \end{aligned} \tag{3.18}$$

Where h_0 and h_{-2} are the white noise and random walk noise coefficients for the clock's Allan variance in the frequency domain. Some typical values for different kinds of oscillators are reported in Table 3.1.

Table 3.1: Clock's variance power spectral density coefficients for various oscillators [24, 25].

Clock type	$\boldsymbol{h_0}$	$\boldsymbol{h_{-2}}$
Ovenized crystal	8×10^{-20}	4×10^{-23}
Rubidium	2×10^{-20}	4×10^{-29}
CSAC	7.2×10^{-21}	2.7×10^{-27}

The Chip Scale Atomic Clock (CSAC) [26] has been included in this comparison because it is a game-changing off-the-shelf solution for precision timing. It approaches the accuracy levels of large atomic clocks while being contained in a single chip. It is therefore expected to be employed in the VULCAIN mission.

It is worth stressing how crucial precise clock synchronization is. In Fig. 3.3 is possible to see the time history of a clock's drift for different timing standards in the temporal window given by a typical LEO orbit. Even if it seems to be dealing with negligible discrepancies, the pseudorange error they would cause is impressively high and can reach a value of several kilometres with the presented drifts, as represented in Fig. 3.3 c. Clock bias is thus the most significant source of error in GNSS positioning, requiring it to be solved every time a position solution is computed.

From the trends in Fig. 3.3, it is easy to understand that a correction to clocks error shall also be implemented in the absence of GNSS covering, and a possible strategy is presented in Sec. 4.4.2.

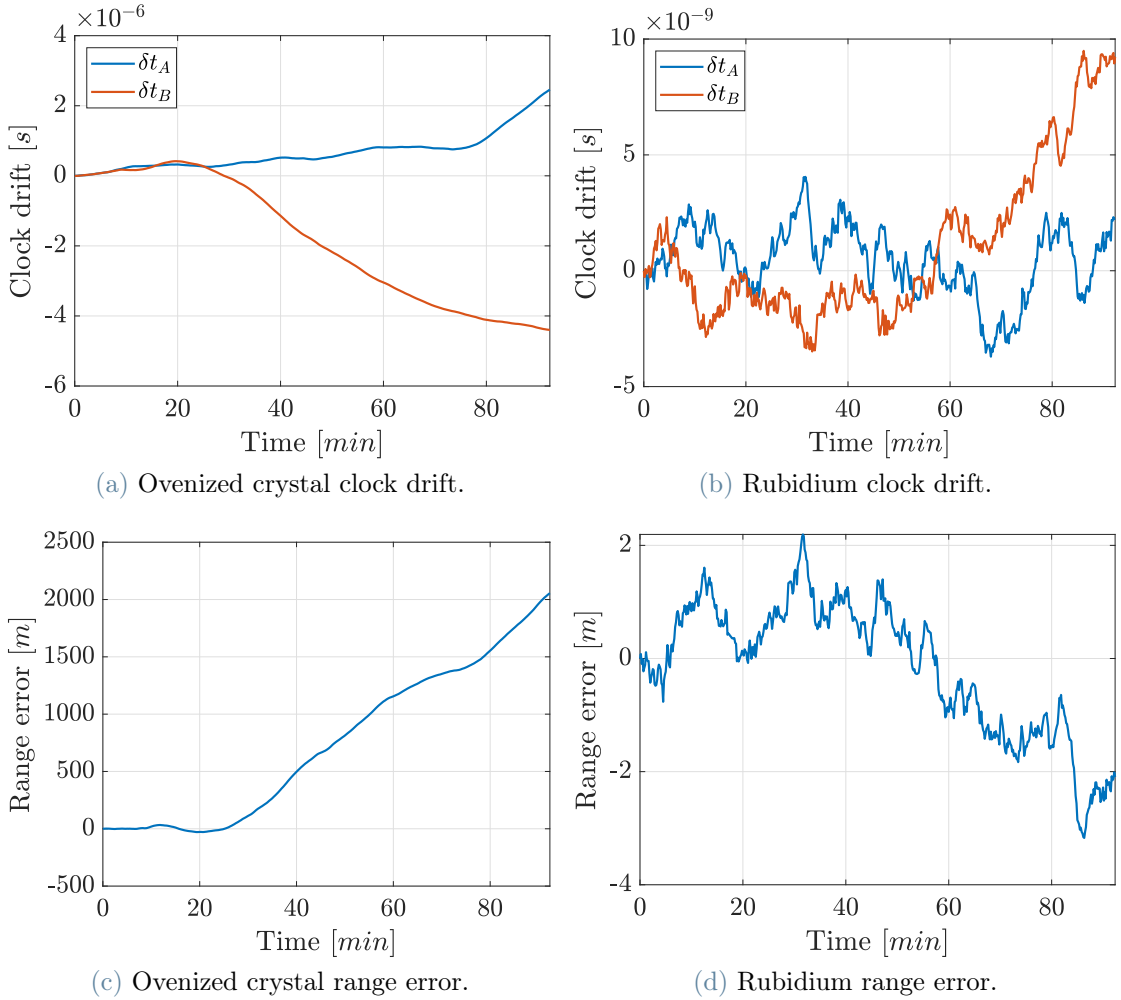

(a) Ovenized crystal clock drift.

(b) Rubidium clock drift.

(c) Ovenized crystal range error.

(d) Rubidium range error.

Figure 3.3: Clock drifts for different oscillator technologies and range errors introduced by them occurring in the time span of a LEO orbit.

3.2.5. Ionospheric interactions model

As already seen, the ionosphere is a critical source of error for GNSS applications. The induced perturbations stem from the ionosphere's composition. At heights between 100 and 1000 km, atmospheric gases are ionized by incoming UV light from the Sun, increasing the density of charged particles. This density is highly variable between day and night and is strongly influenced by solar activity, whose prediction on a short time scale is known to be challenging.

At typical GNSS frequencies, the parameter that affects propagation the most is the Total Electron Content (TEC) of the ray's path. In particular, it is computed as the integrated number of electrons encountered by the signal from its transmission to its reception points.

$$TEC_{AB} = \int_{\mathbf{r}_A}^{\mathbf{r}_B} N_{e^-}(\mathbf{r})\, d\mathbf{r} \tag{3.19}$$

The TEC is involved in the computation of the ionospheric refractive index since a first-order approximation of the Appleton-Hartree equation reads:

$$n = 1 - \frac{40.3}{f^2} TEC_{AB} \tag{3.20}$$

As seen from Eq. (3.20), the refractive index varies with the frequency. This property defines the ionosphere as a dispersive medium and causes a different propagation velocity for the group and phase of RF waves. In particular, for signals at typical GNSS frequencies, this leads to an increased phase velocity and a reduced group velocity. Since modulated information like PRN codes is propagating with the group velocity, there will be an additional delay when measuring pseudorange (see Eq. (3.8)). Conversely, the carrier waves travel with the phase velocity, leading to a phase advance (see Eq. (3.16)).

Finally, an estimate for ionospheric electron content is needed to complete the discussion of ionospheric effects. One of the most widely used models is the International Reference Ionosphere (IRI). It is an empirical model that provides values for electron density and other valuable quantities for a specified geographic location, time, and date. It employs experimental coefficients obtained worldwide through periodic ionospheric radio sounding and uses solar and geomagnetic indices to refine the model. In Fig. 3.4 is possible to see a typical electron density distribution at LEO altitudes obtained through an IRI run.

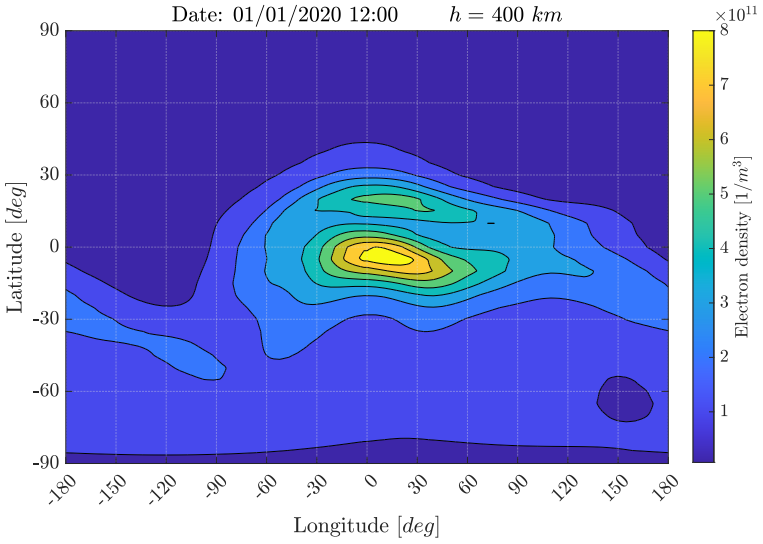

Figure 3.4: Ionospheric electron density at 400 km height.

3.3. Dynamic models for relative navigation

There are several ways to describe the motion of two or more spacecraft flying in a formation, whose modeling accuracy depends on the application under consideration. The leading player in this choice is the nominal baseline or inter-satellite distance.

Relative-based approach For close-range formations ($d \approx 10\ km$) in near-circular orbits, a relative description of motion with the Clohessy-Wiltshire linear model (CW) allows a fair accuracy while maintaining computational cost very low [27]. This model allows both a Cartesian and a Relative Orbital Elements (ROE) formulation, with the latter extending its applicability to formations with larger along-track separations.

The main advantage of this description is that it provides an analytical insight into the relative dynamics, which is very helpful while studying system properties from a theoretical point of view (e.g. observability) or for formation design and control purposes.

The drawbacks are related to the inability to incorporate perturbations effortlessly due to the need to retrieve an expansion of differential accelerations in terms of the relative state itself and the fact that for larger baselines, the nonlinearity becomes more and more predominant.

Several alternatives to the CW model have been proposed to increase its domain of applicability to more general orbits, which is the case of the Yamanaka-Ankersen model for elliptical orbits [28], or to include various perturbations [4].

Absolute-based approach On the other hand, nonlinear numerical models can handle a wider variety of configurations while offering the possibility of including perturbations in the model straightforwardly.

In this case, the description of motion is treated from an absolute point of view by using the two-body problem nonlinear equation in the ECI or ECEF reference frames. When choosing an ECEF-based description of motion, care must be taken to include all the non-inertial terms that stem from rotating frames.

Each spacecraft trajectory is propagated independently, and the relative state is retrieved by subtraction. Moreover, high-precision integration allows a coherent implementation considering the typical accuracy of, for example, GNSS measurements, which can nowadays approach the decimeter level [29].

Concluding, a real-time general-purpose navigation filter should opt for this class of models whenever the available computational power allows doing so.

State vector Moreover, the state of the formation can equivalently be described in two ways. In the first one, the formation state is described with the absolute quantities of each spacecraft and the relative motion is computed as the difference between absolute states. In this case, the dynamics is represented as described in Eq. (3.21).

$$\mathbf{x} = \begin{Bmatrix} \mathbf{r}_A \\ \mathbf{v}_A \\ \mathbf{r}_B \\ \mathbf{v}_B \end{Bmatrix} \qquad \mathbf{x}(t) = \mathbf{x}(t_0) + \int_{t_0}^{t} \begin{Bmatrix} \mathbf{v}_A(\tau) \\ \mathbf{a}_A(\tau,\, \mathbf{r}_A,\, \mathbf{v}_A) \\ \mathbf{v}_B(\tau) \\ \mathbf{a}_B(\tau,\, \mathbf{r}_B,\, \mathbf{v}_B) \end{Bmatrix} d\tau \tag{3.21}$$

The alternative description is based on the absolute state of one spacecraft augmented with the relative state. With this formulation, which allows operating explicitly with relative quantities, the integration is performed as expressed by Eq. (3.22).

$$\mathbf{x} = \begin{Bmatrix} \mathbf{r}_A \\ \mathbf{v}_A \\ \boldsymbol{\Delta}\mathbf{r}_{AB} \\ \boldsymbol{\Delta}\mathbf{v}_{AB} \end{Bmatrix}$$

$$\mathbf{x}(t) = \mathbf{x}(t_0) + \int_{t_0}^{t} \begin{Bmatrix} \mathbf{v}_A(\tau) \\ \mathbf{a}_A(\tau,\, \mathbf{r}_A,\, \mathbf{v}_A) \\ \boldsymbol{\Delta}\mathbf{v}_{AB}(\tau) \\ \mathbf{a}_B(\tau,\, \mathbf{r}_A + \boldsymbol{\Delta}\mathbf{r}_{AB},\, \mathbf{v}_A + \boldsymbol{\Delta}\mathbf{v}_{AB}) - \mathbf{a}_A(\tau,\, \mathbf{r}_A,\, \mathbf{v}_A) \end{Bmatrix} d\tau \tag{3.22}$$

Orbital perturbations The more refined the model is, the more expensive it will be from a computational point of view. In particular, a trade-off between accuracy and computational cost shall be performed to decide which perturbation to include and which not. Three approaches are available when dealing with perturbations depending on the driving need, as summarized in Table 3.2.

It is common in the literature to adopt a so-called reduced dynamics approach. In this framework, only the most significant perturbations are modelled, while the others are estimated as empirical accelerations. These latter are embedded in the state vector in

Table 3.2: Orbital perturbations handling strategies.

Method	Accuracy	CPU cost
Model	High	High
Estimate	Low	Medium
Neglect	None	None

the form of first-order Gauss-Markov processes. This practice also allows the employment of lower fidelity models since the empirical accelerations could catch every imperfection resulting in unmodeled perturbations.

All the remaining modelling uncertainties can be accounted for by increasing the associated process noise in the navigation filter.

4 | Navigation Filter Implementation

After reviewing all the ranging techniques and selecting the most promising ones for a CubeSat application, an implementation of their measurement models within an **Extended Kalman Filter for a two-spacecraft formation** is now proposed. Although many alternatives are possible, the intention is to create a simple and versatile tool that can be used, through appropriate simulations, to assess the performances of different navigation strategies.

In particular, the following chapters will investigate different ranging techniques, the impact of delayed measurements, and the effectiveness of error mitigation strategies.

4.1. Reference frames

In the following chapters, two reference frames will be adopted to describe the two-spacecraft formation for which this navigation filter is designed.

As represented in Fig. 4.1, the reference frames are:

- **Earth-Centered Inertial - ECI:** coordinate frame which has its origin at the centre of mass of Earth and is fixed with respect to the stars. The x-axis is aligned with the mean equinox. The z-axis is aligned with the Earth's rotation axis or celestial North Pole. The y-axis is rotated by 90° East about the celestial equator.
- **Local-Vertical Local-Horizontal - LVLH:** coordinate frame which originates at the master spacecraft's centre of mass and depends on its position in orbit. The x-axis is aligned with the local radial direction. The y-axis lies on a plane normal to the x-axis and is aligned with the velocity projection on that plane. The z-axis is normal to the x and y axes.

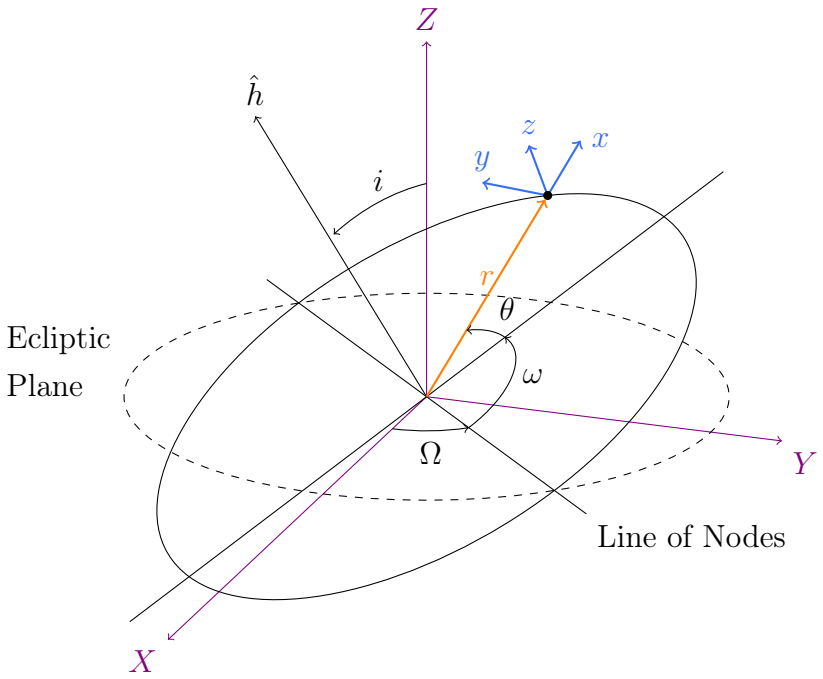

Figure 4.1: Reference frames representation: — ECI, — LHLV

An orthogonal rotation matrix can be derived from the dynamics model to rotate vector quantities from one frame to another:

$$\boldsymbol{A}_{I/L} \qquad \text{Inertial} \quad \rightarrow \quad \text{LVLH}$$

Unless otherwise specified, absolute quantities will be measured in the ECI frame, while relative quantities will be measured in the LVLH frame.

4.2. Filter dynamics & State vectors

The filter's dynamics is expressed by an absolute-based nonlinear model expressed in the ECI frame. The equations of motion are those from the unperturbed two-body problem, with the addition of empirical accelerations.

$$\begin{cases} \ddot{\mathbf{r}}_A = -\dfrac{\mu}{\mathrm{r}_A^3}\,\mathbf{r}_A + \mathbf{a}_A^{\mathrm{emp}} \\ \ddot{\mathbf{r}}_B = -\dfrac{\mu}{\mathrm{r}_B^3}\,\mathbf{r}_B + \mathbf{a}_B^{\mathrm{emp}} \end{cases} \tag{4.1}$$

Where μ is the Earth's gravitational parameter. The state vector is hence in the form:

$$\mathbf{x} = \mathbf{x}_{\text{abs}} = \left\{ \mathbf{r}_A, \mathbf{v}_A, \mathbf{a}_A^{\text{emp}},\ \mathbf{r}_B, \mathbf{v}_B, \mathbf{a}_B^{\text{emp}} \right\}_{\text{ECI}}^T \tag{4.2}$$

Once the absolute state is known, it is possible to obtain the relative one by difference, following the procedure illustrated by Curtis [30]. The relative state thus reads:

$$\mathbf{x}_{\text{rel}} = \left\{ \mathbf{r}_{\text{rel}}, \mathbf{v}_{\text{rel}}, \mathbf{a}_{\text{rel}}^{\text{emp}} \right\}_{\text{LVLH}}^T \tag{4.3}$$

The employment of this model allows the filter to be used in very different scenarios with varying baselines. It also suits the VULCAIN mission's needs, featuring a nominal inter-satellite distance of 150 km with reconfigurability requirements. Moreover, it allows straightforwardly to perform the GNSS measurement update. Finally, it provides flexibility at input and output levels, meaning that it can operate with both absolute and relative measurements and deliver both kinds of state estimates.

Orbital perturbation models have not been included because, as already said, this filter aims to provide a tool for performance assessment and system design rather than an optimized implementation for precise onboard navigation. However, an estimate of their value is computed and exploited in the model via empirical accelerations, lumping all the accelerations apart from the main gravitational term.

4.2.1. State time update

Filter's state time update is performed differently for deterministic and stochastic states. For the state variables whose evolution follows Eq. (4.1), the time update is accomplished through the state transition function $\mathcal{F}(\mathbf{x})$ defined in Eq. (4.5).

Expressing the deterministic sub-state derivative as:

$$\dot{\mathbf{x}}\left(\mathbf{x}, t\right) = \left\{ \mathbf{v}_A, \ddot{\mathbf{r}}_A, \mathbf{v}_B, \ddot{\mathbf{r}}_B \right\}^T \tag{4.4}$$

The state transition function can be written as follows:

$$\hat{\mathbf{x}}_k^{(-)} = \mathcal{F}\left(\hat{\mathbf{x}}_{k-1}^{(+)}\right) = \hat{\mathbf{x}}_{k-1}^{(+)} + \int_{t_{k-1}}^{t_k} \dot{\mathbf{x}}\left(\hat{\mathbf{x}}_{k-1}^{(+)}, \tau\right) d\tau \tag{4.5}$$

As already anticipated, trajectory propagation requires the integration of the equations

of motion.

Conversely, the stochastic part of the state, namely the empirical accelerations, follows a discrete time update. The time evolution of a first-order Gauss-Markov process is given by:

$$\mathbf{a}_k^{\text{emp}} = m(\Delta t)\,\mathbf{a}_{k-1}^{\text{emp}} = e^{-\frac{\Delta t}{\tau}}\,\mathbf{a}_{k-1}^{\text{emp}} \tag{4.6}$$

Once the state's two subgroups have been updated, the state is reordered accordingly to the structure presented in Eq. (4.2).

4.2.2. State covariance time update

Similarly, the state covariance entries related to its deterministic and stochastic parts follow different dynamics in the time update.

Considering the dynamics of the deterministic states ($\mathbf{r}$ and $\mathbf{v}$), recalling Eq. (4.5), it is possible to retrieve the following first-order approximation.

$$\hat{\mathbf{x}}_k^{(-)} = \mathcal{F}\left(\hat{\mathbf{x}}_{k-1}^{(+)}\right) \approx \hat{\mathbf{x}}_{k-1}^{(+)} + \dot{\mathbf{x}}\left(\hat{\mathbf{x}}_{k-1}^{(+)}\right)\Delta t \tag{4.7}$$

The deterministic part of the state transition matrix is hence obtained trivially by deriving Eq. (4.7), yielding:

$$\boldsymbol{F}_{k-1} = \left.\frac{\partial \mathcal{F}}{\partial \mathbf{x}}\right|_{\hat{\mathbf{x}}_{k-1}^{(+)}} = \boldsymbol{I} + \Delta t \left.\frac{\partial \dot{\mathbf{x}}}{\partial \mathbf{x}}\right|_{\hat{\mathbf{x}}_{k-1}^{(+)}} \tag{4.8}$$

Instead, the empirical accelerations are propagated through Eq. (4.6). Thus, to complete the state transition matrix formulation, $\boldsymbol{F}_{k-1}$ is augmented with the rows and columns deriving from this latter operation, whose value will be $m(\Delta t)$.

The covariance update follows the usual equation:

$$\boldsymbol{P}_k^{(-)} = \boldsymbol{F}_{k-1}\boldsymbol{P}_{k-1}^{(+)}\boldsymbol{F}_{k-1}^T + \boldsymbol{Q} \tag{4.9}$$

Where $\boldsymbol{Q}$ is the process noise covariance matrix of the proposed EKF. In this design, only the empirical accelerations have an associated process noise in the following form, while the other terms are set to zero.

$$q_a = \sigma_a^2 \left(1 - m^2(\Delta t)\right) \tag{4.10}$$

Where σ_a^2 is the steady-state variance.

This approach has been chosen because the integration of $\mathbf{r}$ is exact, while the one of $\mathbf{v}$ is not, but all of its uncertainty has been lumped in the empirical acceleration terms that enter the dynamics as described in Eq. (4.1).

4.3. Measurement update

This EKF design includes two measurement types: GNSS measurements and inter-satellite pseudorange. The former are used to perform indirect ranging, thanks to data exchange via ISL as described in Sec. 3.2.2. The latter are obtained by the GNSS-like direct ranging technique introduced in Sec. 3.2.3, exploiting once again the ISL.

Measurement update is performed at the first filter iteration following their arrival and decoding. The detailed implementation is presented in the following two sections.

From now on, the discussion will be tailored for the EKF running on spacecraft A that processes, in addition to its own measurements, also the ones transmitted by spacecraft B via ISL.

4.3.1. GNSS update

The GNSS receivers onboard both spacecraft periodically produce a measurement package structured as the one modelled by Eq. (3.2).

While the measurements taken by GNSS receiver A are available immediately, those of GNSS receiver B will be available after an amount of time equal to the transmission delay, quantified by Eq. (3.6). For this reason, assuming that both receivers output their navigation solution at the same instant, which is also synchronized with a filter's update, only the measurement from A will be available for processing at that iteration. Those from B will be processed at the subsequent iteration, introducing an error since spacecraft B will keep moving during this waiting time. A graphical representation of the measurement collection timeline is presented in Fig. 4.2.

Once a new measurement is available during a filter's update, the measurement correction operation is performed as follows.

Denoting with the subscript G the GNSS-related quantities, the state's measurement

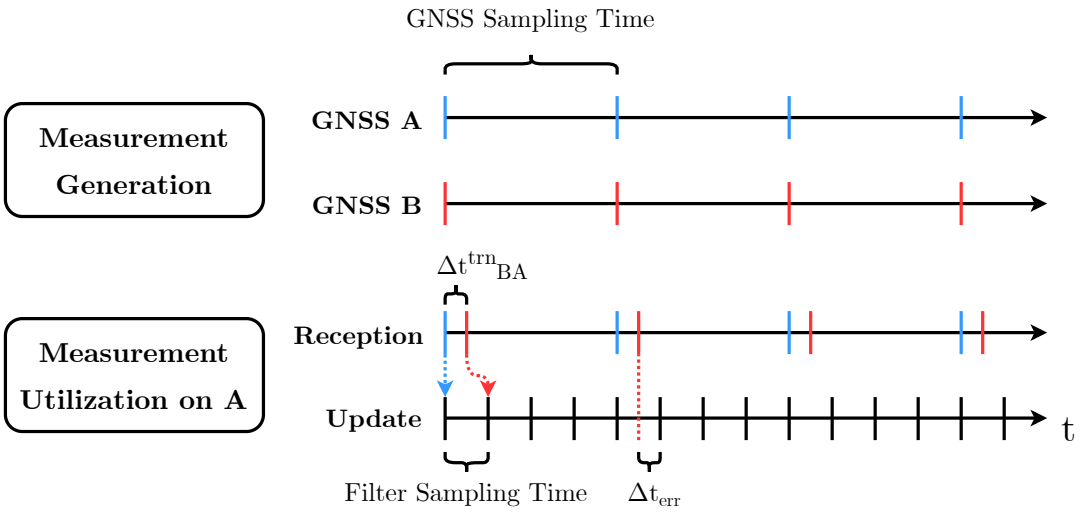

Figure 4.2: Timeline of measurement production, reception and usage compared to filter's update rate.

update is:

$$\boldsymbol{K}_{G\,k} = \boldsymbol{P}_k^{(-)}\,\boldsymbol{H}_G^T\,\left[\boldsymbol{H}_G\boldsymbol{P}_k^{(-)}\boldsymbol{H}_G^T + \boldsymbol{R}_G\right]^{-1} \tag{4.11}$$

$$\hat{\mathbf{x}}_k^{(+)} = \hat{\mathbf{x}}_k^{(-)} + \boldsymbol{K}_{G\,k}\,\left[\mathbf{y}_{G\,k} - \boldsymbol{H}_G\,\hat{\mathbf{x}}_k^{(-)}\right] \tag{4.12}$$

Where:

$$\mathbf{y}_{G\,k} = GNSS_{A,B\,k} = \begin{bmatrix}\mathbf{r}_{A,B}^{ECI}\\ \mathbf{v}_{A,B}^{ECI}\end{bmatrix}_{t_k}$$

is the measurement vector from GNSS receiver A or B at time t_k, in the form of Eq. (3.2);

$$\boldsymbol{H}_{G_A} = [\boldsymbol{I}_{6\times6}\,,\ \mathbf{0}_{6\times12}]$$
$$\boldsymbol{H}_{G_B} = [\mathbf{0}_{6\times9}\,,\ \boldsymbol{I}_{6\times6}\,,\ \mathbf{0}_{6\times3}]$$

are the linear time-invariant observation matrices. Since this measurement update is linear with respect to the state, these are constant.

Finally, the state covariance update is performed in Joseph's form, characterized by better numerical properties.

$$\boldsymbol{P}_k^{(+)} = [\boldsymbol{I}_{18\times18} - \boldsymbol{K}_{G\,k}\boldsymbol{H}_G]\,\boldsymbol{P}_k^{(-)}\,[\boldsymbol{I}_{18\times18} - \boldsymbol{K}_{G\,k}\boldsymbol{H}_G]^T + \boldsymbol{K}_{G\,k}\,\boldsymbol{R}_G\,\boldsymbol{K}_{G\,k}^T \tag{4.13}$$

For GNSS measurements, the covariance matrix reads:

$$\boldsymbol{R}_G = \begin{bmatrix} \boldsymbol{\Sigma}_{\mathbf{r}} & \mathbf{0}_{3\times3} \\ \mathbf{0}_{3\times3} & \boldsymbol{\Sigma}_{\mathbf{v}} \end{bmatrix} \tag{4.14}$$

Where the block diagonal entries are the position and velocity covariance matrices of the employed GNSS receiver.

4.3.2. Inter-Satellite pseudorange update

Inter-Satellite pseudoRange (ISR) measurements can be obtained in almost real-time and at a higher rate than GNSS ones. They are less demanding from a computational point of view since they require a single correlation and nearly no additional operations.

In One-Way Ranging mode, each spacecraft generates a ranging signal that the other receives and exploits to compute the pseudorange. The actual observable is thus not exact, but it contains all the errors already seen in its measurement model (see Sec. 3.2.1.1).

In this case, the measurement update function is nonlinear and to compute the observation matrix it needs to be linearized at each iteration around the current estimate. However, an analytical expression for the Jacobian can be employed to reduce the computational burden.

The derivation starts by writing the nonlinear measurement function employed in the filter:

$$\hat{y}_\rho = h\left(\mathbf{x}\right) = \left[\mathbf{r}_B - \mathbf{r}_A\right]^T \left[\mathbf{r}_B - \mathbf{r}_A\right] \tag{4.15}$$

This expression picks up only the main term of the pseudorange measurement model presented in Eq. (3.8), treating all the error components as measurement noise. Moreover, the inter-satellite distance is considered squared inside the function. Doing this, the square root associated with distance computation vanishes, leading to a simpler linearization. It can be shown that the desired Jacobian reads:

$$\boldsymbol{H}_{\rho\,k} = \left.\frac{\partial h}{\partial \mathbf{x}}\right|_{\hat{\mathbf{x}}_k^{(-)}} = 2\left[\hat{\mathbf{r}}_{B\,k}^{(-)} - \hat{\mathbf{r}}_{A\,k}^{(-)}\right]^T \left[-\boldsymbol{I}_{3\times3}\,,\ \mathbf{0}_{3\times6}\,,\ \boldsymbol{I}_{3\times3}\,,\ \mathbf{0}_{3\times6}\right] \tag{4.16}$$

Finally, the measurement update is performed once again by following equations (4.11)

– (4.13), but, in this case, measurements are given by $y_{\rho\,k} = \rho_k^2$, the observation matrix is $\boldsymbol{H}_{\rho\,k}$ and needs to evaluated at each iteration using Eq. (4.16). The measurement covariance is scalar and is denoted by the following:

$$\boldsymbol{R}_\rho = \sigma_\rho^2 \tag{4.17}$$

4.4. Error mitigation strategies

In order to identify a strategy for error reduction, it is first necessary to understand which terms cause the most significant deviations.

Considering indirect ranging, the only error, apart from the AGWN, is transmission delay. As explained in Sec. 4.3.1, this introduces a discrepancy between the actual position of spacecraft B during the filter's iteration and the one contained in the measurement vector employed for the contextual state update.

Regarding ISR, its measurement model shows several terms, but the most significant is by far the one involving clock biases. Moreover, the ionospheric delay, especially in periods of intense solar activity, might play an influential role.

Therefore, the following three sections will be devoted to discussing possible strategies that allow a noteworthy reduction of the errors stemming from these phenomena.

4.4.1. Transmission delay handling

The idea behind this correction technique is that GNSS measurements have the same structure and especially the same dynamics as state variables. Hence, it means that it is possible to use the filter's dynamics model to propagate an outdated measurement until the time at which it needs to be used for state update.

This approach is made possible because each GNSS receiver time tags every solution as soon as it is computed. Once a measurement needs to be used in the state measurement update step, its timestamp is compared to the current filter's time. If the difference is higher than a certain threshold, the measurement and its covariance are propagated for that precise amount of time. A flowchart of the process is presented in Fig. 4.3.

Since propagation intervals are generally small, this allows using high precision, up-to-date measurements also in the presence of significant transmission delays.

This technique has been implemented within the filter's GNSS measurements update step,

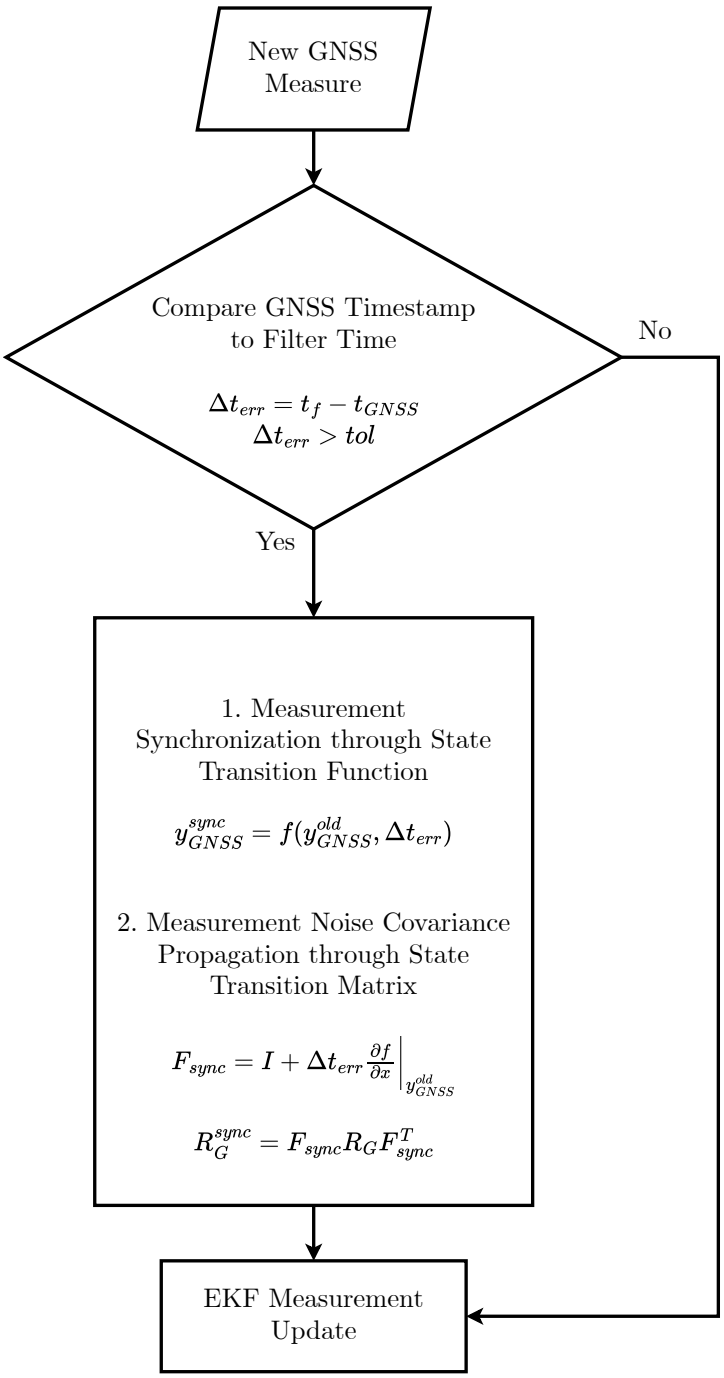

Figure 4.3: Block scheme of the measurement propagation technique.

leading to the improvements that will be later discussed in Sec. 6.2.2.2.

4.4.2. Clock bias correction

Every clock has its drift, meaning it cannot precisely measure time over prolonged periods. This behaviour is not of particular concern under GNSS constellations coverage since the

batch estimation employed by commercial receivers is designed to solve for both position and clock bias, allowing a synchronization precise to the nanosecond level. It is much more challenging (and interesting) to address this problem in all the situations in which timing shall be performed autonomously onboard.

A clever solution can come from the availability of an ISL. In particular, by exploiting the properties of ranging measurements and the possibility of performing Dual One-Way Ranging, it is possible to compute a position estimate almost independent of clock biases and, in the meantime, obtain an estimate of the bias itself.

These statements can be demonstrated by recalling the pseudorange measurement model, here expressed for signal transmission from satellite B to A in a form that lumps all the errors apart from clock bias in a single deviation term.

$$\rho_{BA}(t) = |\mathbf{r}_A(t) - \mathbf{r}_B(t - \Delta t_{BA}^{trn})| + c\,(\delta t_A - \delta t_B) + \delta\rho_{BA} \tag{4.18}$$

If, at the same instant, also satellite B can compute the pseudorange exploiting signals coming from satellite A its measurement would be:

$$\rho_{AB}(t) = |\mathbf{r}_B(t) - \mathbf{r}_A(t - \Delta t_{AB}^{trn})| + c\,(\delta t_B - \delta t_A) + \delta\rho_{AB} \tag{4.19}$$

Supposing that a spacecraft can process both the ranging measurements, it is possible to form the DOWR observable by averaging two quasi-synchronous OWRs.

$$\begin{aligned}
\rho_{\mathrm{DOWR}}(t) &= \frac{\rho_{AB}(t) + \rho_{BA}(t)}{2} \approx \\
&\approx \frac{|\mathbf{r}_B(t) - \mathbf{r}_A(t - \Delta t_{AB}^{trn})| + |\mathbf{r}_A(t) - \mathbf{r}_B(t - \Delta t_{BA}^{trn})|}{2} + \frac{\delta\rho_{AB} + \delta\rho_{BA}}{2} \\
&\approx |\mathbf{r}_A(t) - \mathbf{r}_B(t - \Delta t_{BA}^{trn})| + \frac{\delta\rho_{AB} + \delta\rho_{BA}}{2}
\end{aligned} \tag{4.20}$$

In the sum, clock biases vanish, yielding a result which is the mean of the OWR pseudoranges, corrupted by the mean of their errors. Since a very similar geometric range is expected, the expression can be further simplified.

An estimate of the clocks bias can be conversely obtained from the difference between the OWRs.

$$\begin{aligned}\delta t_{\mathrm{DOWR}}(t) &= \frac{\rho_{BA}(t) - \rho_{AB}(t)}{2} \approx \\ &\approx \frac{c\,(\delta t_A - \delta t_B) - c\,(\delta t_B - \delta t_A)}{2} + \frac{\delta\rho_{BA} - \delta\rho_{AB}}{2} \\ &\approx c\,(\delta t_A - \delta t_B) + \frac{\delta\rho_{BA} - \delta\rho_{AB}}{2}\end{aligned} \tag{4.21}$$

In this case, the difference makes the almost identical geometric ranges vanish, leading to an expression depending on clock bias only.

4.4.3. Ionospheric correction

The ionospheric interactions with pseudorange and carrier-phase measurements give rise to two opposite effects: group delay and phase advance, already introduced in Sec. 3.2.5.

Since the contributions are equal in magnitude but opposite in sign, they vanish when summed. This feature has been exploited in the GRAPHIC (GRoup And PHase Ionospheric Correction) measurement, allowing an ionosphere-free ranging for single-frequency systems.

$$\rho_{\mathrm{GRAPHIC}} = \frac{1}{2}\,(\rho + \Phi) \tag{4.22}$$

Where ρ is the pseudorange measurement modeled by Eq. (3.8) and Φ the carrier-phase from Eq. (3.16).

Other compensation techniques include using a dual-frequency ranging method or embedding in the filter a simplified position-dependant model for the TEC to estimate the ionospheric delay.

5 | Simulation Framework

This chapter will present the simulation framework used to assess the performances of the proposed EKF. In particular, the test scenario is represented by the VULCAIN mission baseline described in Sec. 1.2. Thus, Secs. 5.1 and 5.2 are devoted to a model for ground-truth dynamics and accurate measurement simulation. Finally, Sec. 5.3 introduces the comparison methods used for performance evaluation.

5.1. Ground-truth dynamics

The adopted test scenario is taken from the VULCAIN mission. In particular, it features two identical 12U CubeSat flying on the same Low Earth Orbit (LEO) with an along-track separation of 150 km. The initial orbital parameters for both spacecraft are reported in Table 5.1. The orbit is a circular 400×400 km LEO.

Table 5.1: Orbital parameters of formation-flying spacecraft.

S/C	$\boldsymbol{a}$ $[km]$	$\boldsymbol{e}$ [-]	$\boldsymbol{i}$ $[deg]$	$\boldsymbol{\Omega}$ $[deg]$	$\boldsymbol{\omega}$ $[deg]$	$\boldsymbol{\theta}_0$ $[deg]$
A	6771	0	97.05	180	0	0
B	6771	0	97.05	180	0	1.27

With these initial orbital parameters, it is possible to compute the initial relative state referred to the ECI frame, reported in Eq. (5.1). It has the same structure as the one in Eq. (4.2).

$$\mathbf{x}_{abs\ 0}^{ECI} = \left\{ \begin{bmatrix} -6771.00 \\ 0.00 \\ 0.00 \end{bmatrix} km, \begin{bmatrix} 0.00 \\ 0.94 \\ 7.61 \end{bmatrix} km/s, \begin{bmatrix} -0.0087 \\ 0.00 \\ 0.00 \end{bmatrix} km/s^2, \right.$$
$$\left. \begin{bmatrix} -6769.34 \\ 18.41 \\ 148.86 \end{bmatrix} km, \begin{bmatrix} 0.17 \\ 0.94 \\ 7.61 \end{bmatrix} km/s, \begin{bmatrix} -0.0087 \\ 0.00 \\ 0.00 \end{bmatrix} km/s^2 \right\} \quad (5.1)$$

The ground-truth states are thus obtained by high-fidelity numerical propagation of the above-described orbits, which are integrated separately. The orbital model includes the following perturbations:

- **Spherical harmonic gravity:** higher order geopotential accelerations up to 120^{th} degree are taken into account through EGM2008 gravitational model;
- **Atmospheric drag:** is taken into account through a cannonball model with the drag coefficient $C_D = 2.2$. Surface area is computed from typical CubeSats dimensions. Atmospheric density has been modelled through the NRLMSISE-00 atmosphere model;
- **Solar radiation pressure:** it has been considered through the model introduced by Wie [31]. It considers momentum variations by absorbed and reflected photons on the spacecraft's exposed surfaces. Geometrical dimensions are those of 12U CubeSats with deployable solar panels. Attitude dynamics has not been simulated, and it is assumed to be nadir-pointing;
- **Third body:** the gravitational attraction of the Moon and Sun have been included. Moon and Sun positions have been computed through planetary ephemerides.

The propagation is performed following an absolute approach in the ECI frame. Once the absolute states are available, the relative ones can be computed following the procedure described by Curtis and then rotated to the LVLH frame. The resulting orbits are represented in Fig. 5.1.

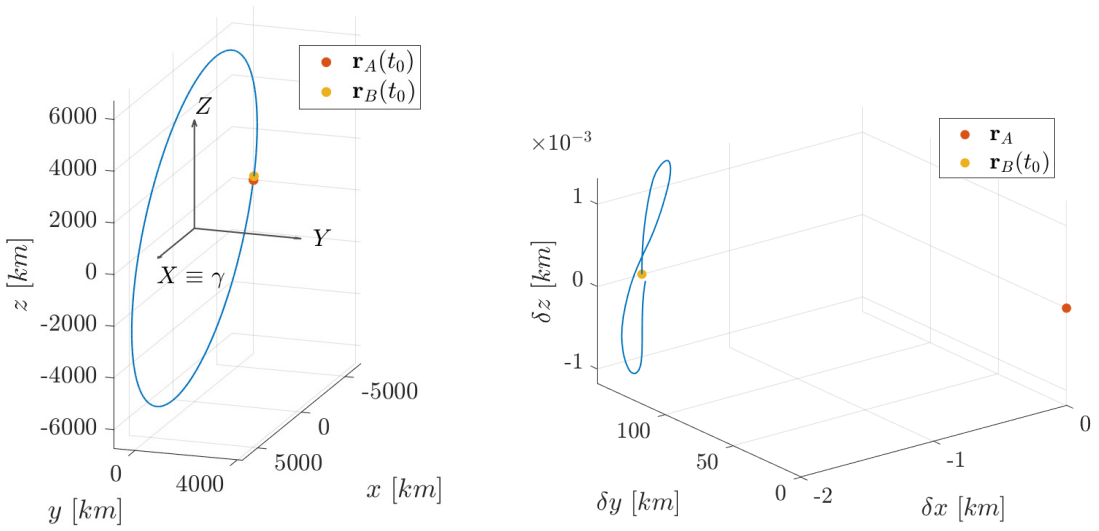

(a) Absolute orbit in the ECI frame.

(b) Relative orbit in the LVLH frame.

Figure 5.1: Representation of absolute and relative spacecraft ground-truth orbits.

5.2. Measurements simulation

The measurements used in the EKF state update are computed following their measurement models developed in Sec. 3.2.

All the time-varying quantities in those equations derive from the ground-truth dynamics propagation. They are corrupted according to their error models, sampled at the desired frequencies and then passed to the filter.

The measurements that suffer from transmission delays are made available to the filter only after the prescribed time has elapsed.

5.2.1. GNSS measurements

GNSS measurements are simulated following Eq. (3.2). In Table 5.2, each term of the measurement equation is reported along with its value and source. Different noise realizations have been used to corrupt measurements for spacecraft A and B.

The receiver's performance data have been taken by the product sheet of the NovAtel OEM719 [32], a Commercial-Off-The-Shelf (COTS) receiver suitable for CubeSat applications. To account for performance degradation in orbit, the original σ values have been multiplied by a conservative safety factor, yielding those reported in the table.

A typical GNSS position history generated with this procedure is presented in Fig. 5.2.

Table 5.2: GNSS measurements simulation parameters.

Term	Description	Value	Source
$\mathbf{r}_{A,B}^{ECI}$	position vector	$f(t)$	ground-truth
$\mathbf{v}_{A,B}^{ECI}$	velocity vector	$f(t)$	ground-truth
t	measurement timestamp	$f(t)$	ground-truth
$\sigma_{\mathbf{r}}$	position accuracy SD*	150 m	OEM719 datasheet [32]
$\sigma_{\mathbf{v}}$	velocity accuracy SD	1 m/s	OEM719 datasheet [32]
σ_t	time sync accuracy SD	2 μs	OEM719 datasheet [32]
Δt_G^s	GNSS sampling time	60 s	user-defined

* Standard Deviation.

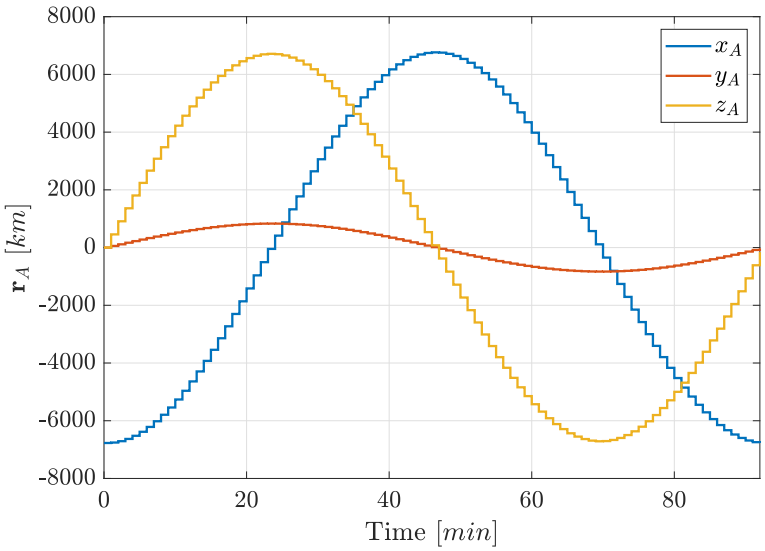

Figure 5.2: Simulated GNSS position history for spacecraft A.

5.2.2. Pseudorange measurements

Pseudorange measurements have been generated through Eq. (3.8). They feature a higher sampling rate and also a higher noise level compared to GNSS measurements. In Table 5.3, each term of the measurement equation is reported along with its value and source. Different noise realisations have been used to corrupt measurements for the two spacecraft.

A brief comment is now made on the parameters presented in the table.

A proper calibration procedure can compensate for line delay by measuring and removing the bias it introduces. Therefore, the one reported here is a small value that can model

Table 5.3: Pseudorange measurements simulation parameters.

Term	Description	Value	Source
Measurement model			**Eq. (3.8)**
$\mathbf{r}_{A,B}$	position vector	$f(t)$	ground-truth
$\delta t_{A,B}$	clock offset	$f(t)$	clock error model
δt^{ion}	ionospheric delay	$f(t)$	ionosphere model
δt^{ln}	line delay	10 ns	assumed
ε_ρ^{th}	thermal noise	WN*	thermal variance model
Δt_ρ^s	pseudorange sampling time	10 s	user-defined
Clock error model			**Eq. (3.17)**
Δt_k	clock model sampling time	10 s	user-defined
h_0	white noise coefficient	7.2×10^{-21}	CSAC model [25]
h_{-2}	random walk coefficient	2.7×10^{-27}	CSAC model [25]
Ionospheric delay model			**Eq. (3.5)**
f	ISL carrier's frequency	420 MHz	VULCAIN proposal
TEC	total electron content	$f(t)$	computed†, Eq. (3.19)
Thermal noise variance model			**Eq. (3.9)**
t_c	chipping period	0.98 μs	PRN design
B_{DLL}	DLL bandwidth	1 Hz	DLL design
t_{eml}	early-minus-late spacing	$0.2\,t_c$	correlator design
C/N_0	RX carrier-to-noise ratio§	30 $dB\,Hz$	receiver design
t_{acc}	pre-detection integration time	10 ms	DLL design
$\sigma_{\varepsilon_\rho}$	pseudorange thermal noise SD	3.1 m	Eq. (3.9) result

* White Gaussian Noise.
† TEC integration is performed numerically during groud-truth simulation at each time step.
§ Minimum carrier-to-noise ratio that guarantees signal reception.

any uncompensated delay.

The clock's parameters are those of the CSAC clock, which is characterised by high stability and is suitable for CubeSat applications. The resulting clock error history and the range error it introduces are presented in Fig. 5.3.

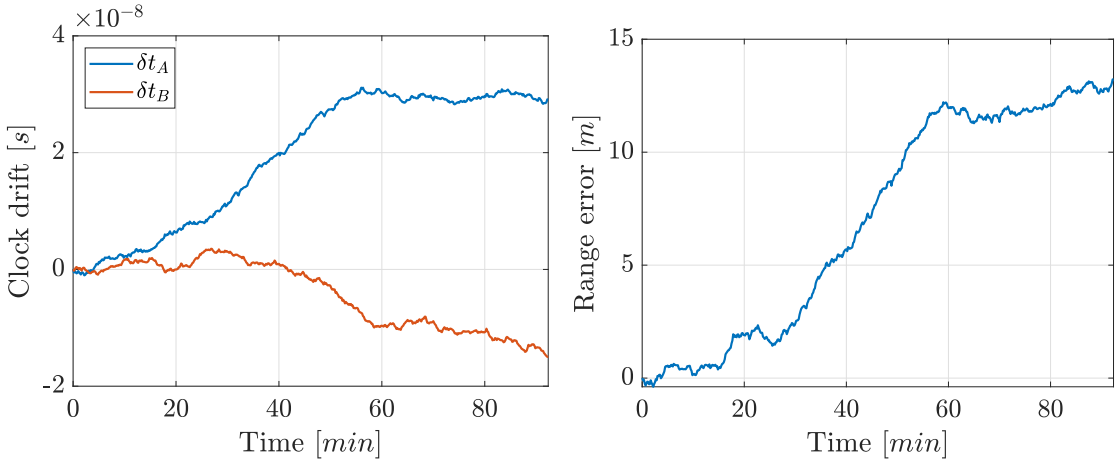

(a) CSAC drift. (b) Drift-induced range error.

Figure 5.3: Simulated CSAC clock's drift and related range error history.

Total Electron Content is computed by numerical integration along the propagation path of the electron density. This latter is, in turn, provided by the IRI model, which outputs a density map for each altitude and simulation date like the one presented in Fig. 3.4. Considering the present scenario, the inter-satellite ionospheric delay history over an orbit is presented in Fig. 5.4.

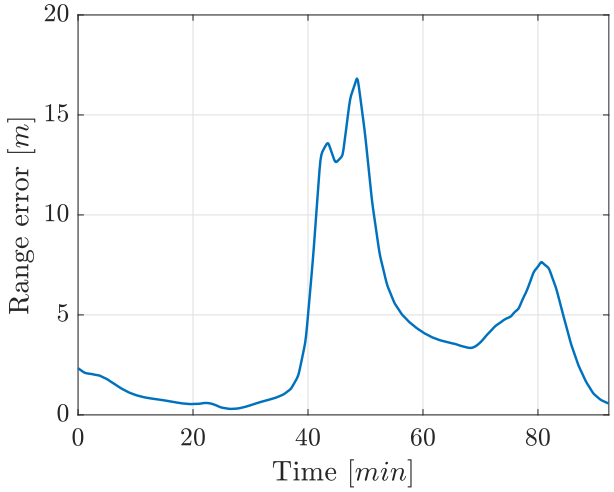

Figure 5.4: Simulated ionospheric delay range error history.

Finally, the thermal noise model depends on the ranging signal receiver's design. In particular, the values reported in Table 5.3 have been assumed by analogy with similar

systems. Moreover, the presented noise standard deviation is the worst-case scenario value since it is computed from the minimum C/N0 ratio that makes the signal decodable. Any higher SNR would lead to better performances.

The time history of the simulated pseudorange over an orbit is represented in Fig. 5.5. A significant noise level characterises it as it is typical of code-ranging measurements.

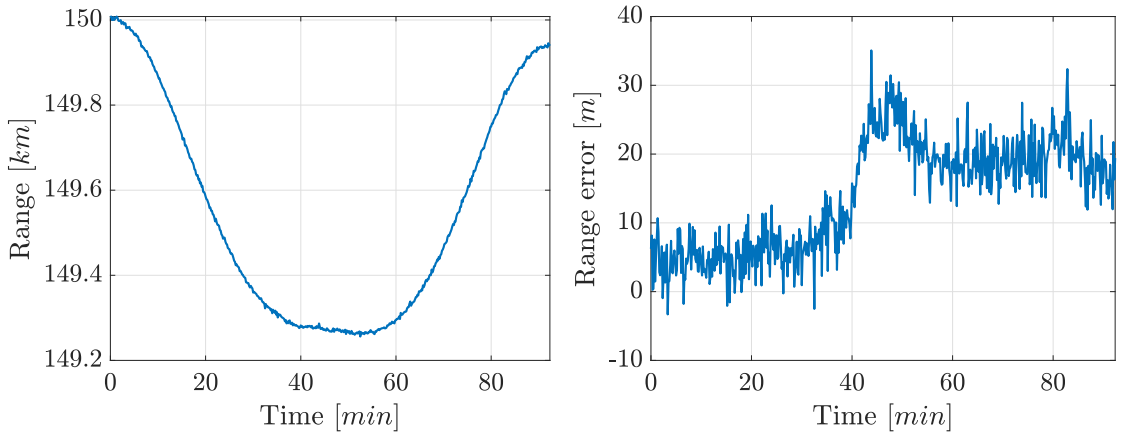

(a) Pseudorange. (b) Pseudorange error.

Figure 5.5: Simulated inter-satellite pseudorange history and its error compared to ground-truth range.

5.2.3. Carrier-Phase measurements

The model for the carrier-phase observable has been introduced in Sec. 3.2.3.2. All the equations and parameters needed to run the simulation are reported in Table 5.4. As usual, different noise realisations are used for the two spacecraft.

In Fig. 5.6, the resulting carrier phase is compared to the simulated pseudorange. As was expected, the resulting measurements show a very low noise level but are also biased due to phase ambiguity. It is interesting to note two things. First, the ionospheric phase advance produces an opposite effect to what happens in pseudorange. Second, albeit being very precise, the phase ambiguity bias does not allow to use carrier-phase as it is since this could cause arbitrarily large errors.

Table 5.4: Carrier-phase measurements simulation parameters.

Term	Description	Value	Source
Measurement model			**Eq. (3.8)**
$\mathbf{r}_{A,B}$	position vector	$f(t)$	ground-truth
$\delta t_{A,B}$	clock offset	$f(t)$	same as pseudorange
λ	ISL carrier's wavelength	71.4 cm	VULCAIN proposal
γ^0	initial receiver's phase	130.58 $cycles$	arbitrarily chosen
ψ^0	initial transmitter's phase	25.42 $cycles$	arbitrarily chosen
δt^{ion}	ionospheric delay	$f(t)$	same as pseudorange
δt^{ln}	line delay	10 ns	assumed
$\delta\phi^{pwu}$	phase windup perturbation	-	neglected*
$\delta\phi^{mp}$	multipath perturbation	WN	mp variance model
$\delta\phi^{pc}$	phase-centre perturbation	WN	pc variance model
ε_ϕ^{th}	carrier-phase thermal noise	WN	thermal variance model
Δt_ϕ^s	carrier-phase sampling time	10 s	user-defined
Multipath variance model			
$\sigma_{\phi^{mp}}$	multipath SD	$(0.005\ m)/\lambda$	empirical estimate [22]
Phase-centre variance model			
$\sigma_{\phi^{pc}}$	phase-centre SD	$(0.01\ m)/\lambda$	empirical estimate [22]
Thermal noise variance model			**Eq. (3.9)**
B_{PLL}	PLL bandwidth	15 Hz	PLL design
C/N_0	RX carrier-to-noise ratio§	30 $dB\,Hz$	receiver design
$\sigma_{\varepsilon_\phi}$	carrier-phase thermal noise SD	14 mm	Eq. (3.9) result

* No angular velocity on antenna boresight in the simulation scenario.
§ Minimum carrier-to-noise ratio that guarantees signal reception.

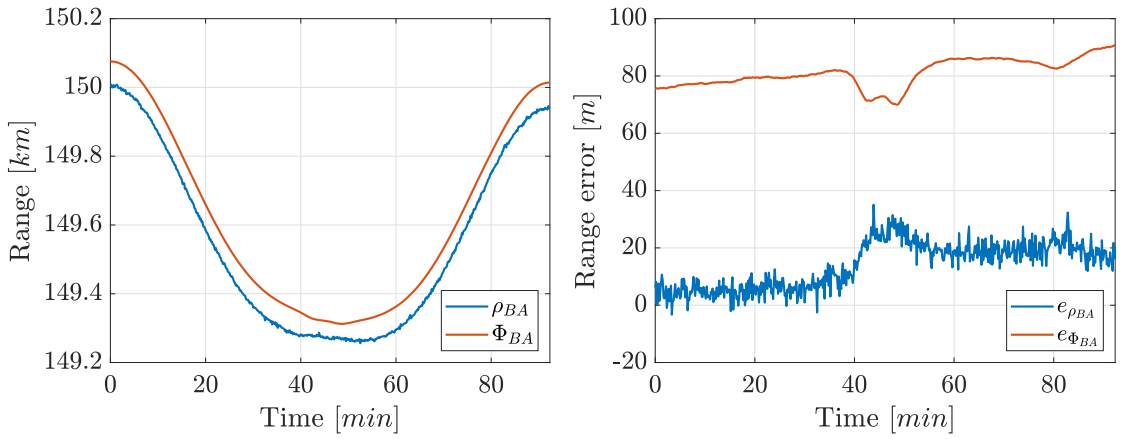

(a) Pseudorange and carrier-phase. (b) Pseudorange and carrier-phase errors.

Figure 5.6: Simulated inter-satellite carrier-phase history and its error compared to ground-truth range. Equivalent plots for pseudorange are overlapped for comparison.

5.3. Performance evaluation procedure

To assess the performances of the proposed EKF, a simulation framework has been developed, as described in this chapter. The comparison flowchart is presented in Fig. 5.7.

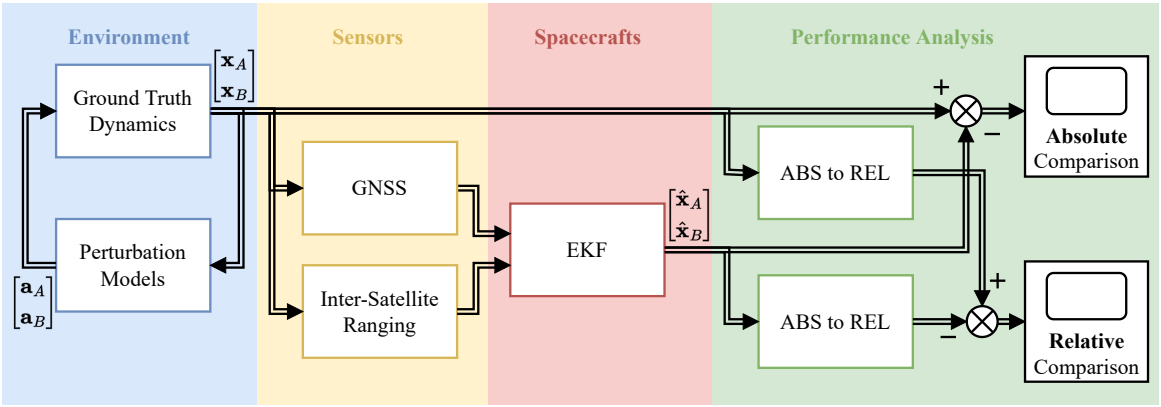

Figure 5.7: Simulation-based performance evaluation flowchart.

At first ground-truth dynamics, from which measurements are synthesised, is simulated. Once available, the EKF starts processing these latter to refine its state estimates. Finally, the estimated state variables (absolute quantities in the ECI frame) are converted to relative quantities in the LVLH frame. This step enables the performance evaluation from an absolute and relative point of view.

Two sets of comparison methods will be used in the following section:

- **Absolute state comparison:** this will be mainly employed to evaluate the con-

vergence of the filter with respect to the ground-truth states. Both actual $\mathbf{x}_{\text{abs}}$, $\hat{\mathbf{x}}_{\text{abs}}$ values and the $\hat{\mathbf{x}}_{\text{abs}} - \mathbf{x}_{\text{abs}}$ difference, namely the absolute estimation error, can be visualised;

- **Relative state comparison:** once convergence has been guaranteed, this approach will be followed to focus on relative navigation performances. Similarly to the absolute case, both actual $\mathbf{x}_{\text{rel}}$, $\hat{\mathbf{x}}_{\text{rel}}$ values and the $\hat{\mathbf{x}}_{\text{rel}} - \mathbf{x}_{\text{rel}}$ difference, namely the relative estimation error, can be visualised. In particular, this latter will be extensively employed to assess the impact of each measurement type and each error reduction technique on the relative navigation performances.

6 | Results & Discussion

This chapter illustrates the result of the comparison procedure described in Sec. 5.3. The filter performances are evaluated in the simulation scenario to assess the impact of the various measurements on navigation accuracy and the effectiveness of error mitigation techniques. Finally, the possibility of performing inter-satellite range-only relative navigation within an EKF formulation is explored.

For the whole discussion, it is helpful to recall that the filter under test is running on spacecraft A, which takes in input measurements from both the spacecraft of the formation.

6.1. Initial settings

The filter runs presented in this chapter have been simulated with the initial conditions described in the following paragraphs. Its sampling time Δt_f is equal to 1 s.

Initial state The initial state vector is built whit the first measurements of the GNSS receivers of spacecraft A and B as soon as they are received and become available to the onboard navigation filter of spacecraft A. The initial state, reported in Eq. (6.1), differs from the true one, in Eq. (5.1), by a tiny amount related to GNSS receiver precision.

$$\hat{\mathbf{x}}_{abs\ 0}^{ECI} = \left\{ \begin{bmatrix} -6770.93 \\ -0.06 \\ -0.17 \end{bmatrix} km, \begin{bmatrix} 0.00 \\ 0.94 \\ 7.61 \end{bmatrix} km/s, \begin{bmatrix} 0 \\ 0 \\ 0 \end{bmatrix} km/s^2, \right.$$
$$\left. \begin{bmatrix} -6769.24 \\ 18.43 \\ 148.90 \end{bmatrix} km, \begin{bmatrix} 0.17 \\ 0.94 \\ 7.61 \end{bmatrix} km/s, \begin{bmatrix} 0 \\ 0 \\ 0 \end{bmatrix} km/s^2 \right\} \quad (6.1)$$

Initial state covariance The initial state covariance $\boldsymbol{P}_0$ has been constructed considering the accuracy of the GNSS measurements used to construct the initial state vector. For the empirical accelerations, the covariance has been taken from the related process noise matrix entry. The result is presented in Eq. (6.2).

$$\boldsymbol{P}_0 = \begin{bmatrix} \boldsymbol{R}_G & \dots & \dots & \mathbf{0} \\ \vdots & \boldsymbol{q}_a & & \vdots \\ \vdots & & \boldsymbol{R}_G & \vdots \\ \mathbf{0} & \dots & \dots & \boldsymbol{q}_a \end{bmatrix}_{18\times 18} \tag{6.2}$$

Process and measurement noise covariance The $\boldsymbol{Q}$ and $\boldsymbol{R}$ matrices involved in the filter have been set according to the default formulation presented in Secs. 4.2 and 4.3. The numerical values for the standard deviations needed are reported in Tables 5.2 to 5.4.

6.2. Filter performances

The results of the performance evaluation procedure are here reported and commented on. The comparison has been performed over one orbit of the chief spacecraft (A), following the process illustrated in Sec. 5.3.

Results are shown for different simulation conditions. In particular, the impact of the various measurements is assessed by starting with filter dynamics propagation only and then adding the available measurements one type at a time. The same is done for some error mitigation techniques illustrated in Sec. 4.4. Both absolute and relative state estimation errors are presented to distinguish better how and where each refinement step acts to improve the navigation accuracy. The notation adopted for this paragraph is reported in Eqs. (6.3) and (6.4).

$$\Delta\mathbf{x}_{\text{abs}} = \hat{\mathbf{x}}_{\text{abs}} - \mathbf{x}_{\text{abs}} = \left\{\Delta\mathbf{r}_A,\ \Delta\mathbf{v}_A,\ \Delta\mathbf{a}_A^{\text{emp}},\ \Delta\mathbf{r}_B,\ \Delta\mathbf{v}_B,\ \Delta\mathbf{a}_B^{\text{emp}}\right\}^T_{\text{ECI}} \tag{6.3}$$

$$\delta\mathbf{x}_{\text{rel}} = \hat{\mathbf{x}}_{\text{rel}} - \mathbf{x}_{\text{rel}} = \left\{\delta\mathbf{r}_{\text{rel}},\ \delta\mathbf{v}_{\text{rel}},\ \delta\mathbf{a}_{\text{rel}}^{\text{emp}}\right\}^T_{\text{LVLH}} \tag{6.4}$$

A summary of all the examined cases is eventually reported at the end of the section.

6.2.1. No measurements

To start the performance evaluation, filter dynamics have been propagated freely (i.e. without adding any information by the sensors). The error tends unsurprisingly to increase since this is a blind propagation without any measurement update. There are two error sources:

- **Wrong initial conditions:** since the initial conditions of the navigation filter, coming from GNSS measurements, are not exact (and thus different from the ground-truth one), the propagated trajectories will follow different paths. These latter will eventually return to the original configuration once per orbit, apart from the deviations given by the perturbations acting on each spacecraft;
- **Poor perturbation model:** the ground-truth model accounts for perturbations while the filter does not, introducing an error which is set to increase with time.

The absolute and relative estimation errors are reported in Figs. 6.1 and 6.2. The two figures show different trends due to the above-cited reasons. While the absolute one tends to increase indefinitely, the relative exhibits more periodic behaviour since it depends much more on initial conditions rather than perturbations. These latter are very similar on the two spacecraft, making their difference low and thus acting on timescales more extended than the simulation time.

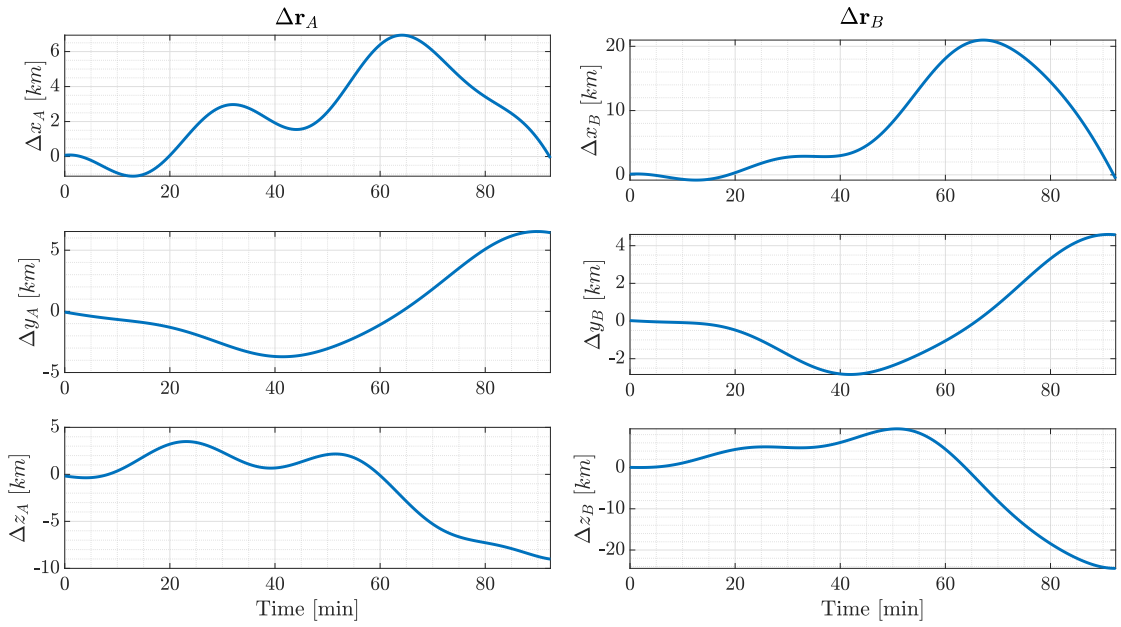

(a) Spacecraft A. (b) Spacecraft B.

Figure 6.1: Absolute position estimation error without any measurement.

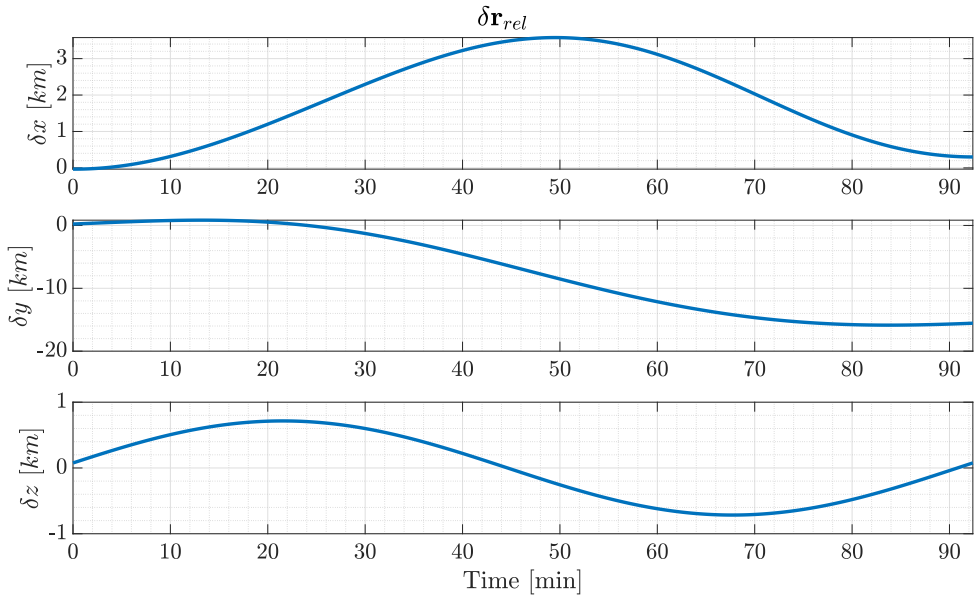

Figure 6.2: Relative position estimation error without any measurement.

6.2.2. GNSS-only

Adding GNSS measurements enable the filter to process an absolute measurement. As a result, the absolute state estimation error decreases considerably compared to the previous case. The update step is described in Sec. 4.3.1.

Two cases are distinguished. In the first one, the measurements from the GNSS receiver of spacecraft B, which can be processed only with a delay equal to the total transmission time, are employed without any manipulations at the first iteration after they have become available. In the second, the synchronisation strategy described in Sec. 4.4.1 is first applied to them.

6.2.2.1. Without synchronization

As can be seen from Fig. 6.3, there is a significant difference between the accuracy improvement experienced by the absolute positions of spacecraft A and B. The first can rely on real-time measurements obtained by its onboard receiver, while the above-cited delay corrupts the second. It is indeed visible that while the first lie perfectly inside the 3σ covariance bounds, the second is significantly outside them, indicating a poor error convergence.

This is even clearer by analysing Fig. 6.4, where it is possible to understand that the use of delayed measurements introduces a bias in the along-track component of the relative position vector. This is compatible with the orbital description of the phenomenon. Being

the leader in an along-track formation, if an *old* measurement is used to correct the position of spacecraft B, this latter will appear to be *behind* its actual position. The estimate of the relative position vector will thus be *shorter* than the true one, yielding a constant bias in the estimation error.

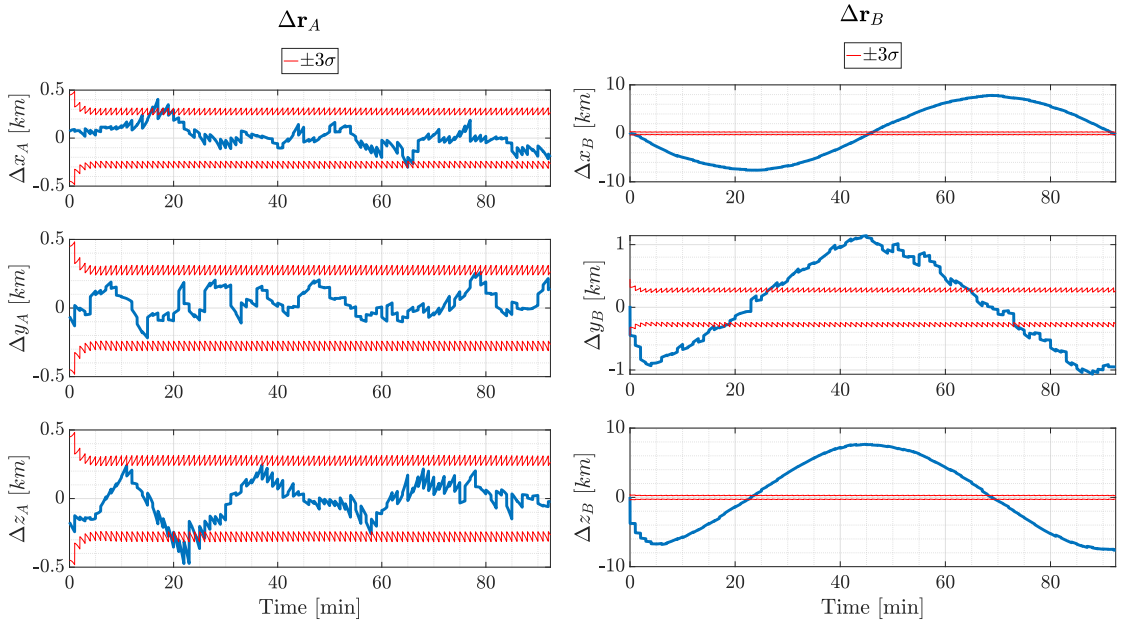

(a) Spacecraft A. (b) Spacecraft B.

Figure 6.3: Absolute position estimation error with GNSS only.

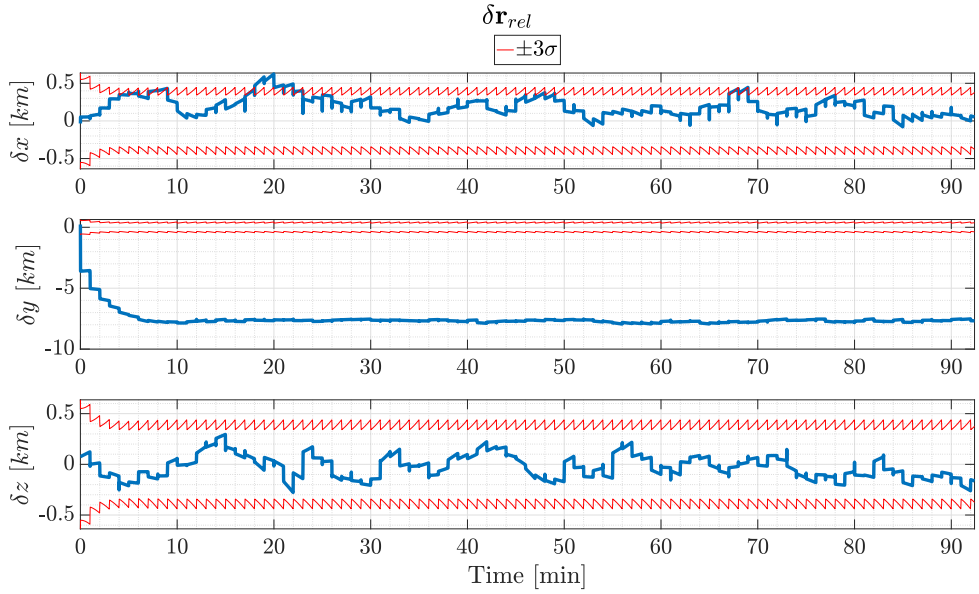

Figure 6.4: Relative position estimation error with GNSS only.

Table 6.1: Mean and standard deviation of the position estimation error components in the GNSS only case.

	Absolute S/C A			Absolute S/C B			Relative		
	Δx_A	Δy_A	Δz_A	Δx_B	Δy_B	Δz_B	δx	δy	δz
$\boldsymbol{\mu}$ $[m]$	17	36	−19	46	31	124	192	−7572	−26
$\boldsymbol{\sigma}$ $[m]$	112	91	132	5389	683	5254	129	562	113

6.2.2.2. With synchronization

The synchronisation technique proposed in Sec. 4.4.1 demonstrates its effectiveness in Figs. 6.5 and 6.6. Applying it to the incoming B measurements, the absolute and relative estimation errors are considerably improved. The former shows comparable precision levels between spacecraft A and B, while the latter's bias in the along-track direction appears to be removed.

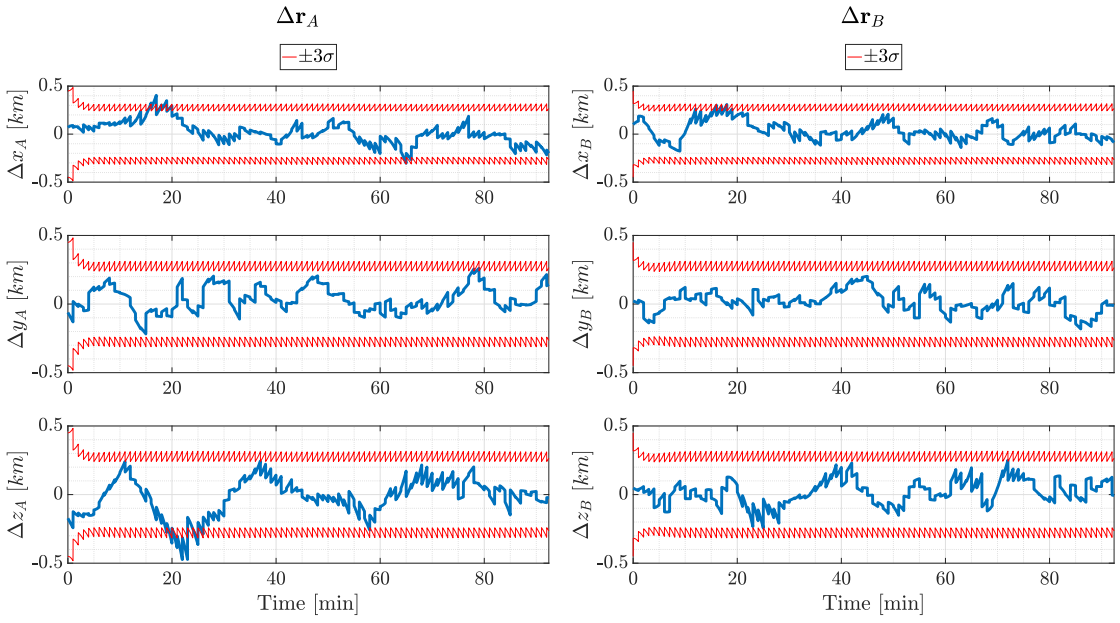

(a) Spacecraft A. (b) Spacecraft B.

Figure 6.5: Absolute position estimation error with GNSS and synchronization.

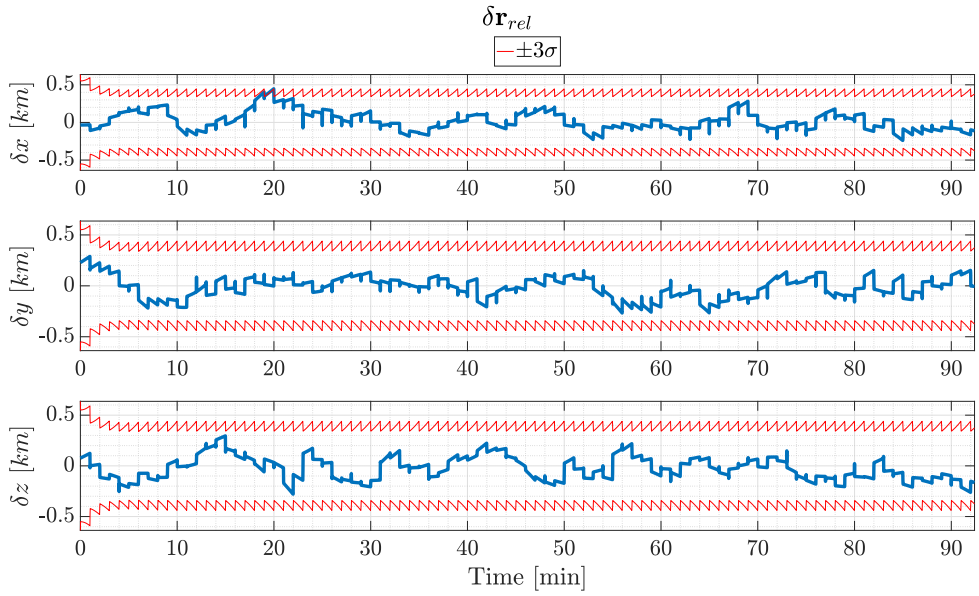

Figure 6.6: Relative position estimation error with GNSS and synchronization.

Table 6.2: Mean and standard deviation of the position estimation error components in the GNSS with synchronization case.

	Absolute S/C A			**Absolute S/C B**			**Relative**		
	Δx_A	Δy_A	Δz_A	Δx_B	Δy_B	Δz_B	δx	δy	δz
$\boldsymbol{\mu}$ $[m]$	17	36	-19	33	16	18	22	-14	-26
$\boldsymbol{\sigma}$ $[m]$	112	91	132	94	76	88	125	104	113

6.2.3. GNSS & inter-satellite pseudorange

Here are presented the results obtained by employing in the measurement update step of the EKF both the synchronised GNSS and the inter-satellite pseudorange observations. Adding a measure of relative nature means that the information it conveys is more suitable for improving the knowledge of the relative state. This can be confirmed by comparing the absolute and relative estimation accuracy enhancements represented respectively in Figs. 6.7 and 6.8. While the second improves considerably, especially in the along-track direction, the first also improves, but very slightly.

Starting from Fig. 6.8 is possible to notice how strongly the along-track component of the relative position vector benefits from the inter-satellite pseudorange. This can be easily explained since the inter-satellite position vector is always aligned with the along-track

direction of the LVLH reference frame in the considered formation. The radial component is dynamically coupled with the along-track one and thus has a side benefit from δy improvements. Conversely, the out-of-plane component is uncoupled and is characterized by low observability. Thus, it is not affected by this measurement in any way.

As already said, there are no substantial refinements to the absolute navigation solution. It is, however, worth noting that the improvements in the along-track relative direction are here spread on all three components of the ECI reference frame. Due to the orientation of the orbital plane, the relative position vector is roughly lying on the x-z plane, meaning that higher effects are foreseen in these directions. The trend in the covariance bounds supports this conclusion.

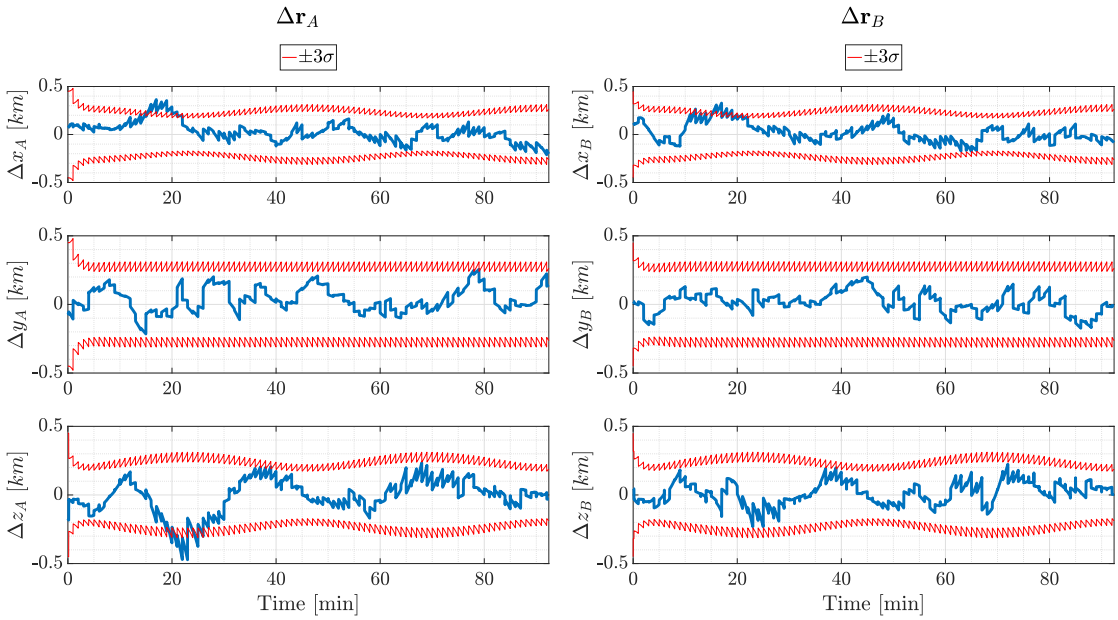

(a) Spacecraft A. (b) Spacecraft B.

Figure 6.7: Absolute position estimation error with GNSS, synchronization and inter-satellite pseudorange.

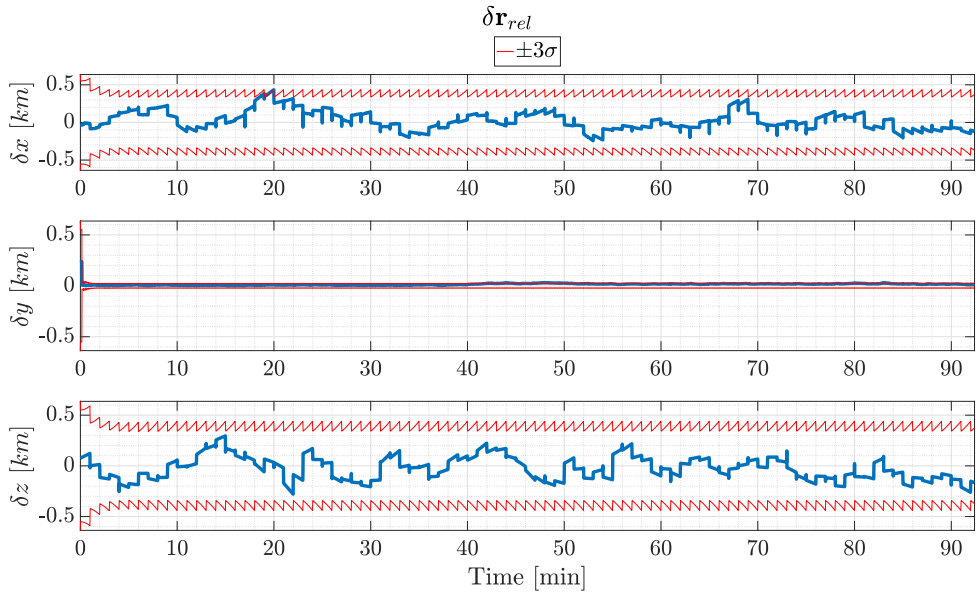

Figure 6.8: Relative position estimation error with GNSS, synchronization and inter-satellite pseudorange.

Table 6.3: Mean and standard deviation of the position estimation error components in the GNSS and inter-satellite pseudorange case.

	Absolute S/C A			**Absolute S/C B**			**Relative**		
	Δx_A	Δy_A	Δz_A	Δx_B	Δy_B	Δz_B	δx	δy	δz
$\boldsymbol{\mu}$ $[m]$	30	37	-13	20	16	13	26	15	-26
$\boldsymbol{\sigma}$ $[m]$	100	89	126	96	76	80	122	12	113

6.2.4. Inter-satellite pseudorange only

It is interesting to analyse the possibility of performing relative navigation with the inter-satellite pseudorange measurements only. This could be the case of a contingency scenario, a deep-space mission, or any other situation in which GNSS-based solutions are unavailable.

The results are presented in Fig. 6.9. Surprisingly, a fair relative state convergence is maintained for the first two components of the relative position vector. Best results are obtained for the along-track component, as it is intuitive to understand considering the above-discussed geometrical reasons. The radial component benefits from being dynamically coupled with δy. Instead, the δz component, characterized by the lowest observability, diverges slightly after 30 minutes.

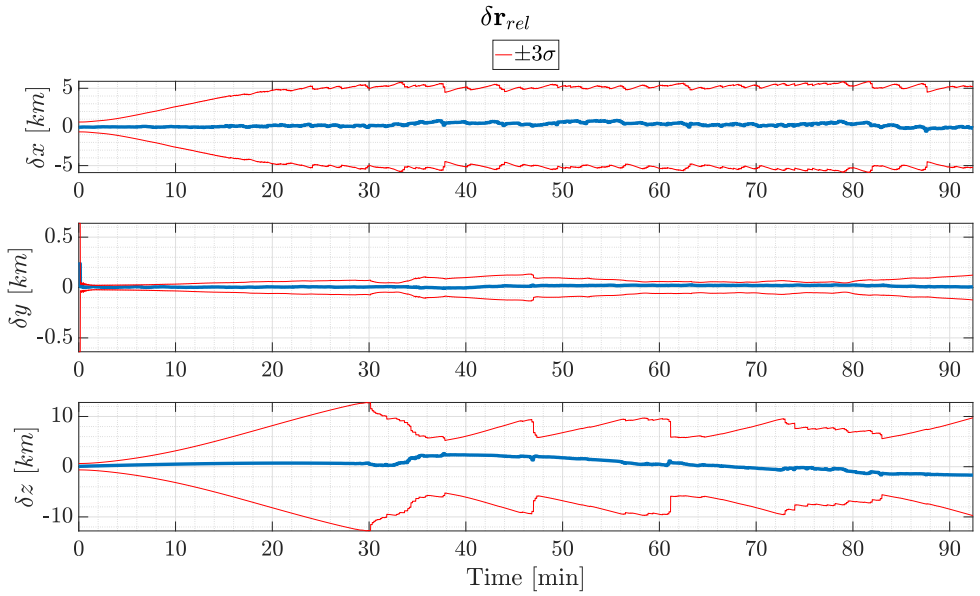

Figure 6.9: Relative position estimation error with inter-satellite pseudorange only.

Table 6.4: Mean and standard deviation of the position estimation error components in the inter-satellite pseudorange only case.

	Relative		
	δx	δy	δz
$\boldsymbol{\mu}$ $[m]$	262	12	463
$\boldsymbol{\sigma}$ $[m]$	250	13	1076

6.2.5. Comparison of the filter performances

The purpose of this section is to present a comparison between the improvements that have been described in each of the previously presented implementations of the EKF. To do so, the relative estimation error of each technique is superimposed on the others, allowing to visualize which are the more significant contributions to navigation accuracy.

What is shown in Fig. 6.10 is thus a summary of the steps taken to arrive at the final navigation baseline, featuring synced GNSS and ISR measurements. As already said, the GNSS synchronization procedure effectively removes the along-track bias. The synchronization hence produces the most significant effects, while adding the ISR impacts only the along-track component of the estimation error.

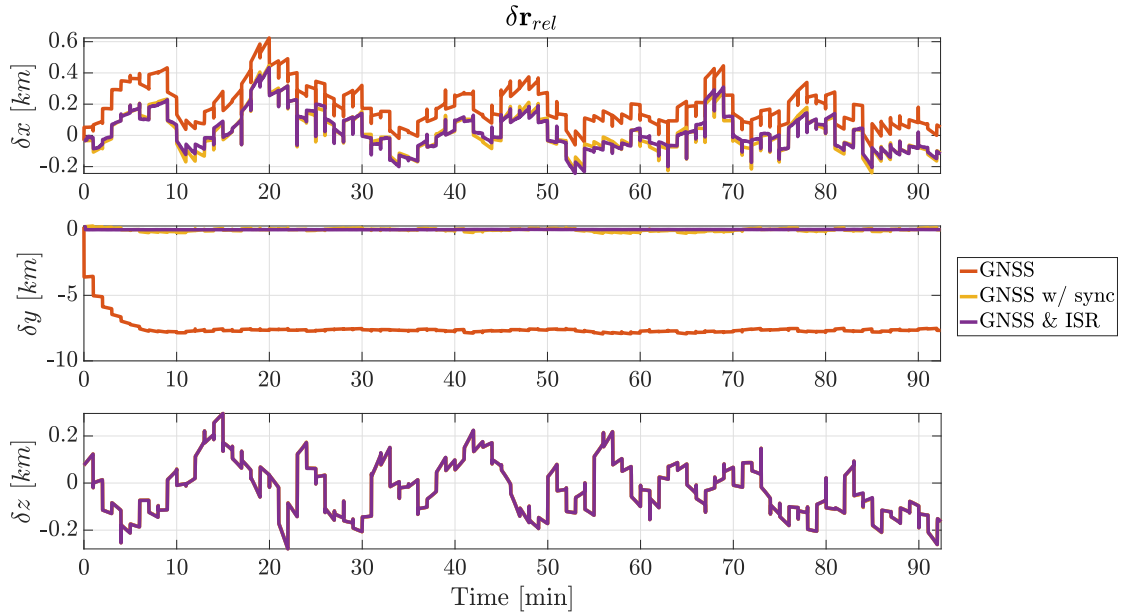

Figure 6.10: Relative position estimation error upgrades with different techniques.

The last comparison, in Fig. 6.11, is devoted to proving that the ISR-only navigation can improve the estimates of δx and, more significantly, δy obtained in a measurement-free propagation. Concerning δz, although slightly worse, its error remains bounded. This allows concluding that ISR-only navigation can represent a valuable solution for relative state determination in the absence of GNSS coverage.

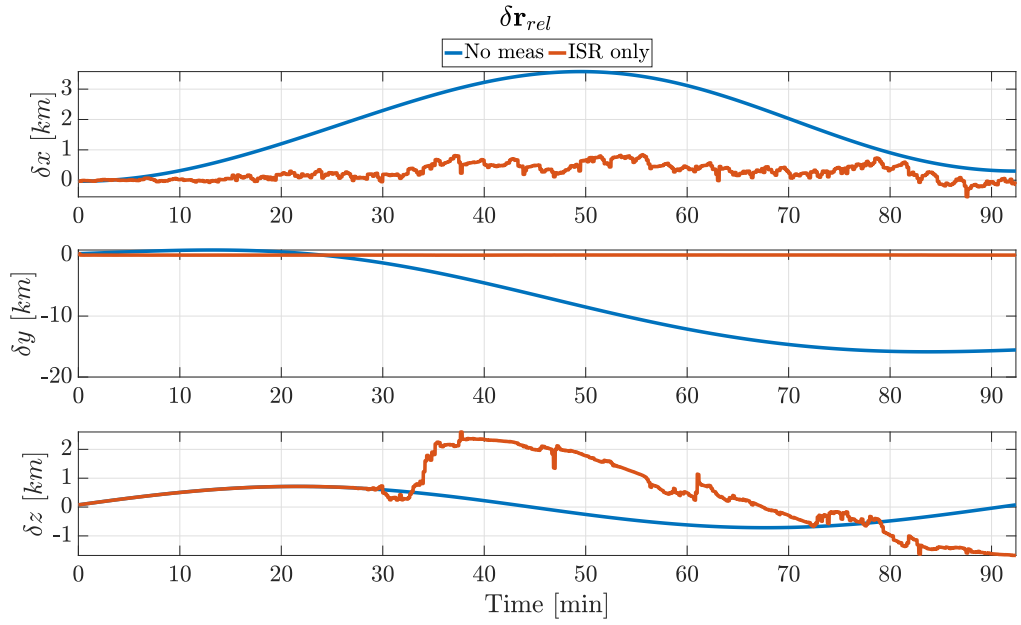

Figure 6.11: Comparison of relative position estimation error in measurement-free propagation and ISR-based navigation.

6.3. Robustness analysis

A Monte Carlo analysis has been performed to verify the algorithm's robustness with respect to initial conditions. In particular, since the initial state and its covariance are uncertain parameters, it is essential to understand whether their variation could cause the filter to diverge. Several realizations of the uncertain variables are obtained by considering the random distributions presented in Table 6.5.

Table 6.5: Uncertain variables distribution around their nominal values for Monte Carlo analysis.

Parameter	$\boldsymbol{\sigma}$	**Distribution**
$\mathbf{r}_{A,B_0}$	1500 m	Gaussian
$\mathbf{v}_{A,B_0}$	10 m/s	Gaussian
$\mathbf{a}^{\text{emp}}_{A,B_0}$	4.1×10^{-3} m/s^2	Gaussian
$\boldsymbol{P}_0$	$0.25^2\, \boldsymbol{P}_0\|_{\text{nominal}}$	Gaussian

The number of Monte Carlo runs has been selected to represent the global statistical response of the filter, following the approach proposed by Hanson [33]. The standard

error of the mean is used to set a reasonable accuracy level to be reached with this analysis. It represents an estimate of how far the time average of a single realization is likely to be found from the ensemble average of all the realizations of the Monte Carlo analysis. It can be approximated as a function of the nominal sample standard deviation σ and the number of runs n.

$$SE \approx \frac{\sigma}{\sqrt{n}} \tag{6.5}$$

Applying the standard error of the mean to $n = 100$ runs of both the nominal case (i.e. the one with synced GNSS and ISR measurements) and the ISR-only one, the results presented in Table 6.6 are obtained. Only these two scenarios are examined from a statistical point of view since they are the most promising ones for respectively nominal and contingency navigation.

Table 6.6: Standard error of the mean for Monte Carlo analysis ($n = 100$).

	GNSS & ISR			**ISR-only**		
	δx	δy	δz	δx	δy	δz
$\boldsymbol{\sigma}$ $[m]$	122.2	11.97	113.2	250.5	12.65	1076
$\boldsymbol{SE}$ $[m]$	12.2	1.2	11.3	25.1	1.3	108

Considering the non-observability of the δz component in the contingency scenario, it is possible to conclude that the Monte Carlo analysis accuracy with $n = 100$ is enough to investigate filter's convergence in case of uncertain initial conditions.

For this purpose, all the runs are visualized in Figs. 6.12 and 6.13. Toghether with the individual samples, the filter's 3σ bounds and the Monte Carlo ensemble 3σ bounds have been reported. These latter have been computed as the ensemble average of the dataset at each time step plus its ensemble standard deviation.

Considering the case in which both GNSS and ISR measurements are processed (cfr. Fig. 6.12), it can be concluded that the filter is robust with respect to uncertain initial state and covariance, since all the realizations converge to the nominal one after ~ 10 minutes. At steady state conditions, the Monte Carlo 3σ bounds fall inside the filter's covariance estimate, meaning that the provided results are conservative.

Conversely, in the ISR-only case, the convergence region is much narrower, as can be seen in Fig. 6.13. In fact, the results show that the filter is not able to deal with initial

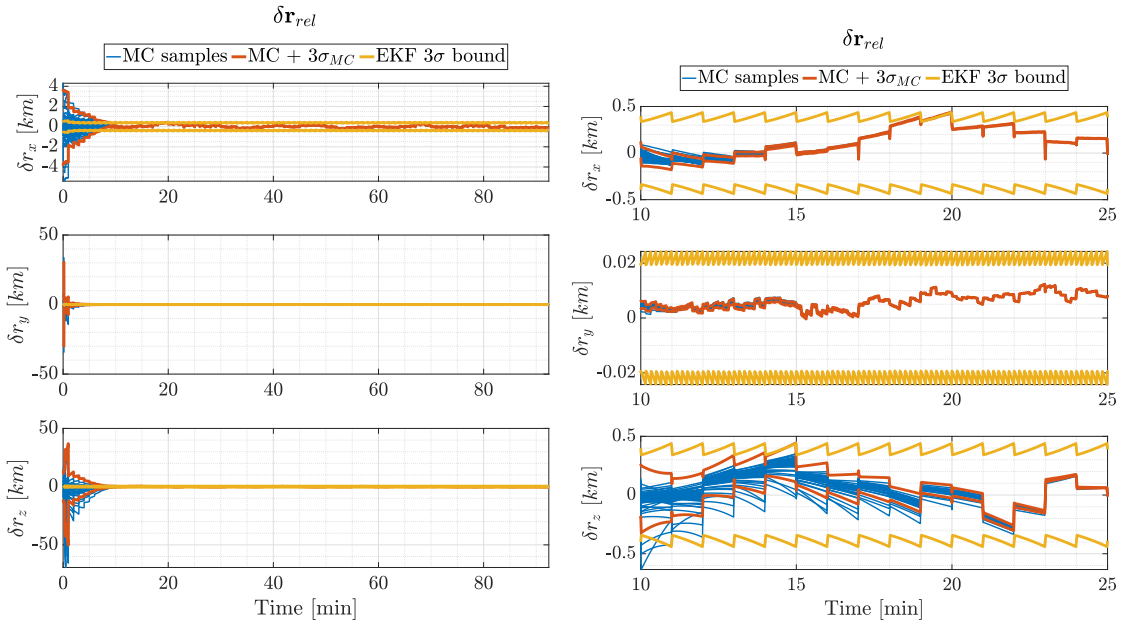

(a) Entire orbit. (b) Zoom on convergence region.

Figure 6.12: Monte Carlo estimation errors for the GNSS & ISR case.

conditions which are too far from the correct ones. This was expected since the relative navigation problem for the formation at hand admits infinite solutions for a given range history, thus preventing it from being observable only with such measurements [34].

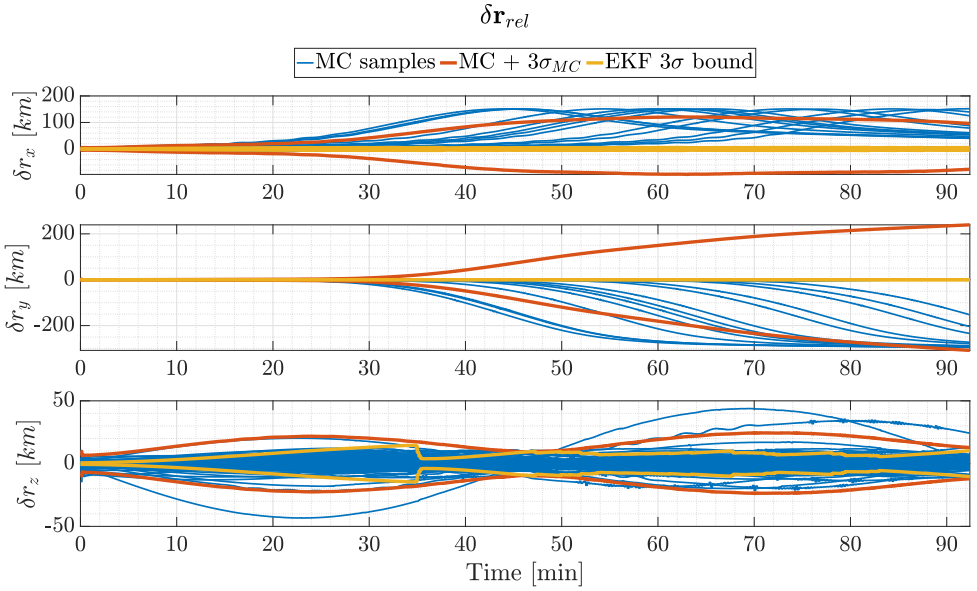

Figure 6.13: Monte Carlo estimation errors for the ISR-only case.

To assess local observability in the same scenario, another Monte Carlo analysis has been run. This time, the standard deviation of the uncertain initial state has been lowered by a

factor of 10 resulting in a σ value of 150 m for the position and 1 m/s for the velocity. The results, reported in Fig. 6.14, demonstrates that the problem is only locally observable. Hence, the possibility of having a reliable ISR-only relative navigation depends strongly on how accurate the initial conditions of the filter are.

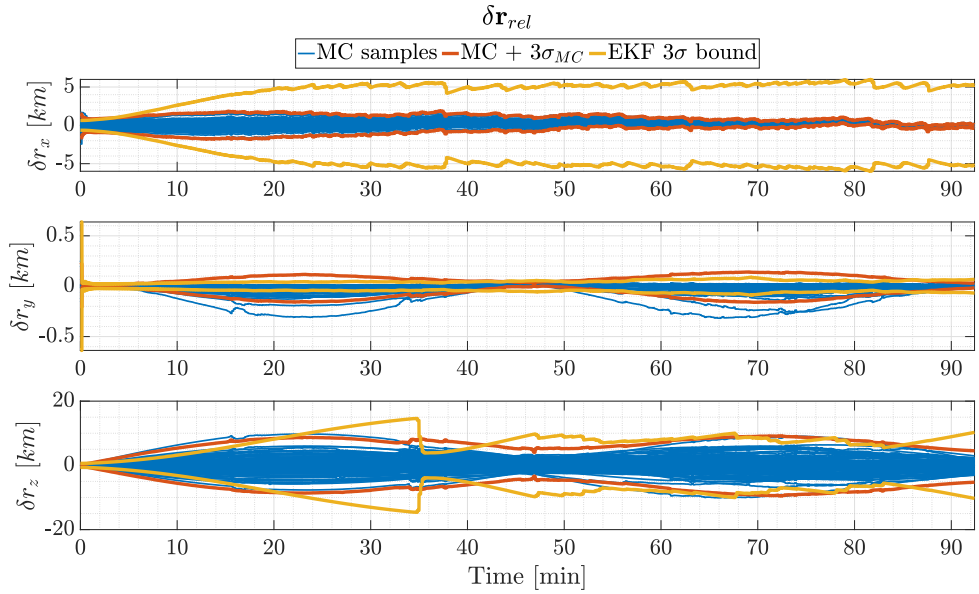

Figure 6.14: Monte Carlo estimation errors for the ISR-only case with lower initial state uncertainty.

7 | Conclusions

What has been presented in Chapter 6 allows concluding that an inter-satellite link in radio frequency can be actively exploited to perform relative navigation, whose accuracy depends on the chosen technique.

In particular, significant findings have been reported in Sec. 7.1. In contrast, Sec. 7.2 is devoted to pointing out what remains to be investigated to move closer to this technology's experimental testing and its actual implementation in a mission like VULCAIN.

7.1. Findings

The following paragraphs summarise what has been noticed through this thesis work and contain the answers to the initial research questions.

Feasibility of ISL-based relative navigation Having reviewed the available ranging techniques, their heritage, the related mathematical models and the simulation results, performing relative navigation onboard is deemed feasible. For this purpose, it is mandatory to establish a communication channel via an inter-satellite link between platforms.

Benefits of GNSS-ISR coupled navigation The impact of adding a ranging measurement to GNSS-based navigation has been proven to be significant. It allows reaching higher precisions in the relative state determination and enhances the system's robustness in case of poor GNSS constellations geometry or unmodeled errors.

Clock accuracy impact The stability of the onboard oscillator has been demonstrated to be a significant concern. Periodic clock corrections shall be foreseen for counteracting the huge positioning errors that this bias would otherwise introduce in the long run. When under GNSS constellations coverage, the receiver can accomplish this task. For different scenarios, an alternative synchronisation procedure shall be designed. The proposed DOWR technique represents a valuable example when employing one-way ranging systems.

Measurement delay impact Using delayed measurements in a filter architecture like the one presented in Chapter 4 has been demonstrated to affect navigation accuracy. Proper strategies shall thus be put in place to correct the bias introduced by these delays. The one proposed in this thesis work has shown to be effective for delayed GNSS measurements.

Feasibility of ISR-only relative navigation The possibility of performing ISR-only relative navigation has been demonstrated for the considered spacecraft formation. This result paves the way for more sophisticated relative navigation techniques independent from external systems, like GNSS or ground-based tracking, that could be attractive for autonomous formation flying missions. For example, this technology can enable unseen scientific possibilities for future deep-space missions.

7.2. Future work

Since the ultimate purpose of this thesis is to lay the foundations for an ISL-based relative navigation system for CubeSat missions, the following sections list what could be the next steps in pursuit of this goal.

Algorithm improvement Concerning the navigation algorithm, additional improvements are expected from the below-presented proposals.

- **Carrier-phase usage:** inter-satellite distance measurements could be further refined using the carrier-phase observable instead of the pseudorange one. To this purpose, the phase ambiguity shall be first estimated through one of the approaches available in the literature, allowing a considerable noise reduction;
- **Ionospheric delay correction:** an ionospheric delay correction method shall be introduced to remove the related bias. Besides the GRAPHIC combination proposed in Sec. 4.4.3, alternative strategies, such as dual-frequency ranging, are available in the literature;
- **Line-of-Sight capabilities:** given the accuracy of the carrier-phase measurements, whose resolution is nearly 1 cm, these latter could also be exploited to perform differential measurements using multiple receiving antennas. Following what is presented in Sec. 2.3, this allows an estimation of the line-of-sight vector of the transmitting antenna. The combined use of ISR and LOS would create a complete set of measurements to perform autonomous relative navigation in every situation, thus overcoming the limitations of ISR-only navigation described in Sec. 6.2.4;

- **Consider alternative designs:** other ranging methods among the ones presented in Sec. 2.3 could be applied to the same scenario, particularly TWR. A model for it should be developed and tested in the algorithm for comparison purposes. Moreover, several ways of performing a GNSS-like direct ranging are available. In particular, the PRN construction, the correlator design, and the carrier's modulation and frequency are all design parameters that are worth to be explored before a final decision is made.

Model refinement The simulation framework fidelity can be enriched by considering the modelling of the following points.

- **RF signal transmission:** the whole RF transmission chain via ISL should be modelled, including PRN generation, modulation and transmission. This would also allow for the accurate computation of the received SNR;
- **RF signal reception:** the RF receiver's frontend and backend simulation shall be performed. This can allow a further understanding of the impact of the signal's de-modulation, correlation procedure, delay and phase tracking loops;
- **Attitude dynamics:** its simulation would yield a better description of multipath and antenna phase centre perturbations. Moreover, the antenna geometry role could be investigated in terms of pointing by selecting the correct directional gain.

Hardware-in-the-loop simulations Once the software design model has reached a higher degree of maturity, some hardware-in-the-loop simulations are needed to validate the promised performances. Moreover, running the navigation filter on space-qualified processors could provide evidence of hidden bottlenecks in the proposed design. Furthermore, a qualification model for the GNSS-like ranging system shall be designed and employed in tests. These shall be conducted with a GNSS signals generator (set for the considered scenario) to simulate all the navigation signals received by both the GNSS and ISR receiver, representing the most realistic testbed before being operated in space.

In conclusion, this thesis represents nothing more than a critical review of what is already available in the literature, carried out with the presented scenario in mind. The purpose of verifying the feasibility of the initial proposal is indeed achieved. Nevertheless, this concept will move forward to its implementation phase only after going through what is suggested in this section. Once deemed mature enough, this system could eventually be considered to navigate the CubeSats formations of the future.

Bibliography

[1] R. Sun, *Relative Nagivation for Satellite Formation Flying based on Radio Frequency Metrology*. PhD thesis, Delft University of Technology, 2014.

[2] R. Sun, J. Guo, D. Maessen, and E. Gill, "Enabling inter-satellite communication and ranging for small satellites," in *Proceedings of the 4S Symposium: Small Satelites, Systems and Services* (s.n., ed.), pp. 1–15, ESA, 2010. Small Satellites, Systems and Services - The 4S Symposium ; Conference date: 31-05-2010 Through 04-06-2010.

[3] M. Marszalek, O. Kurz, M. Drentschew, M. Schmidt, and K. Schilling, "Intersatellite links and relative navigation: Pre-conditions for formation flights with pico- and nanosatellites," *IFAC Proceedings Volumes*, vol. 44, pp. 3027–3032, Jan. 2011.

[4] M. D'Errico, ed., *Distributed space missions for earth system monitoring*, ch. 5-6. Space Technology Library, New York, NY: Springer, 2013 ed., Sept. 2012.

[5] N. Delong, D. Laurichesse, J. Harr, and S. D'Amico, "Prisma relative orbit determination using gps measurements;," in *21st International Symposium on Space Flight Dynamics*, 2009.

[6] G. B. Palmerini, M. Sabatini, P. Gasbarri, L. Schirone, and M. Macellari, "Moderate accuracy relative navigation in formation flying by filtered radio measurements," in *2015 IEEE Aerospace Conference*, pp. 1–7, 2015.

[7] C. L. Sang, M. Adams, T. Hörmann, M. Hesse, M. Porrmann, and U. Rückert, "Numerical and experimental evaluation of error estimation for two-way ranging methods," *Sensors*, vol. 19, p. 616, Feb. 2019.

[8] M. Zink, H. Fiedler, I. Hajnsek, G. Krieger, A. Moreira, and M. Werner, "The tandem-x mission concept," in *2006 IEEE International Symposium on Geoscience and Remote Sensing*, pp. 1938–1941, 2006.

[9] O. Montenbruck, R. Kahle, S. D'Amico, and J.-S. Ardaens, "Navigation and control of the TanDEM-x formation," *The Journal of the Astronautical Sciences*, vol. 56, pp. 341–357, Sept. 2008.

[10] O. MONTENBRUCK, M. WERMUTH, and R. KAHLE, "GPS based relative navigation for the TanDEM-x mission - first flight results," *Navigation*, vol. 58, pp. 293–304, Dec. 2011.

[11] G. Bonin, N. Roth, S. Armitage, J. Newman, B. Risi, and R. E. Zee, "Canx–4 and canx–5 precision formation flight: mission accomplished!," in *Proceedings of the 29th Annual AIAA/USU Conference on Small Satellites*, 2015.

[12] C. Dunn, W. Bertiger, G. Franklin, I. Harris, G. Kruizinga, T. Meehan, S. Nandi, D. Nguyen, T. Rogstad, J. B. Thomas, *et al.*, "The instrument on nasa's grace mission: augmentation of gps to achieve unprecedented gravity field measurements," in *Proceedings of the 15th international technical meeting of the satellite division of the institute of navigation (ION GPS 2002)*, pp. 724–730, 2002.

[13] L. M. Marrero, J. C. Merlano-Duncan, J. Querol, S. Kumar, J. Krivochiza, S. K. Sharma, S. Chatzinotas, A. Camps, and B. Ottersten, "Architectures and synchronization techniques for distributed satellite systems: A survey," *IEEE Access*, vol. 10, pp. 45375–45409, 2022.

[14] D. Kelbel, T. Lee, A. Long, R. Carpenter, and C. Gramling, "Relative navigation algorithms for phase 1 of the mms formation," in *Flight Mechanics Symposium*, 2003.

[15] P. Phung, V. S. Guedeney, and J. Teles, *Tracking and Data Relay Satellite System (TDRSS) Range and Doppler Tracking System Observation Measurement and Modeling.* NASA Goddard spaceflight center, 1980.

[16] S. Bedrich, "Signal design and in-orbit performance of the new microwave satellite tracking system prare," in *1998 IEEE 5th International Symposium on Spread Spectrum Techniques and Applications - Proceedings. Spread Technology to Africa (Cat. No.98TH8333)*, vol. 3, pp. 724–728 vol.3, 1998.

[17] C. Wang and M. Zhou, "Novel approach to intersatellite distance measurement with high accuracy," *Journal of Guidance, Control, and Dynamics*, vol. 38, pp. 944–949, May 2015.

[18] A. Genova and F. Petricca, "Deep-space navigation with intersatellite radio tracking," *Journal of Guidance, Control, and Dynamics*, vol. 44, pp. 1068–1079, May 2021.

[19] E. Kaplan and C. Hegarty, *Understanding GPS/GNSS: Principles and Applications.* Norwood, MA: Artech House, 3 ed., May 2017.

[20] J. Spilker Jr., P. Axelrad, B. W. Parkinson, and P. Enge, eds., *Global Positioning*

System: Theory and Applications, Volume I. American Institute of Aeronautics and Astronautics, Jan. 1996.

[21] J. S. Subirana, J. M. J. Zornoza, and M. H. Pajares, *GNSS data processing.* European Space Agency, 2013.

[22] M. L. Psiaki and S. Mohiuddin, "Modeling, analysis, and simulation of GPS carrier phase for spacecraft relative navigation," *Journal of Guidance, Control, and Dynamics*, vol. 30, pp. 1628–1639, Nov. 2007.

[23] L. Galleani, "A tutorial on the two-state model of the atomic clock noise," *Metrologia*, vol. 45, pp. S175–S182, Dec. 2008.

[24] R. G. Brown and P. Y. C. Hwang, *Introduction to random signals and applied Kalman filtering: with MATLAB exercises and solutions; 3rd ed.* New York, NY: Wiley, 1997.

[25] E. Fernández, D. Calero, and M. Parés, "CSAC characterization and its impact on GNSS clock augmentation performance," *Sensors*, vol. 17, p. 370, Feb. 2017.

[26] Microsemi, "Chip scale atomic clock (CSAC)," 2019.

[27] W. H. CLOHESSY and R. S. WILTSHIRE, "Terminal guidance system for satellite rendezvous," *Journal of the Aerospace Sciences*, vol. 27, pp. 653–658, Sept. 1960.

[28] K. Yamanaka and F. Ankersen, "New state transition matrix for relative motion on an arbitrary elliptical orbit," *Journal of Guidance, Control, and Dynamics*, vol. 25, pp. 60–66, Jan. 2002.

[29] A. Hauschild and O. Montenbruck, "Precise real-time navigation of LEO satellites using GNSS broadcast ephemerides," *NAVIGATION*, vol. 68, pp. 419–432, Apr. 2021.

[30] H. D. Curtis, "Chapter 7 - relative motion and rendezvous," in *Orbital Mechanics for Engineering Students (Third Edition)* (H. D. Curtis, ed.), pp. 367–404, Boston: Butterworth-Heinemann, third edition ed., 2014.

[31] B. Wie, *Space vehicle dynamics and control.* AIAA Education Series, Reston, VA: American Institute of Aeronautics & Astronautics, 2 ed., Sept. 2008.

[32] NovAtel Inc., *NovAtel OEM 719 Product Sheet*, 7 ed., Apr. 2022.

[33] J. M. Hanson and B. B. Beard, "Applying monte carlo simulation to launch vehicle design and requirements verification," *Journal of Spacecraft and Rockets*, vol. 49, pp. 136–144, Jan. 2012.

[34] J. A. Christian, "Relative navigation using only intersatellite range measurements," *Journal of Spacecraft and Rockets*, vol. 54, pp. 13–28, Jan. 2017.

List of Figures

List of Tables

List of Acronyms

Acronym	Description
CDGPS	Carrier-Phase Differential GPS
CW	Clohessy-Wiltshire
DLL	Delay Lock Loop
DOWR	Dual One-Way Ranging
EKF	Extended Kalman Filter
GNSS	Global Navigation Satellite System
GPS	Global Positioning System
ISL	Inter-Satellite Link
ISR	Inter-Satellite Ranging
LOS	Line of Sight
OWR	One-Way Ranging
PRN	Pseudo Random Noise
RF	Radio-Frequency
ROE	Relative Orbital Elements
SAR	Synthetic Aperture Radar
SD	Standard Deviation
TWR	Two-Way Ranging
UHF	Ultra High Frequency
WN	White Noise